

## Analysis of zonal flow pattern formation and the modification of staircase states by electron dynamics in gyrokinetic near marginal turbulence

Cite as: Phys. Plasmas **28**, 072305 (2021); <https://doi.org/10.1063/5.0054358>

Submitted: 17 April 2021 • Accepted: 06 July 2021 • Published Online: 21 July 2021

 F. Rath, A. G. Peeters and  A. Weikl

### COLLECTIONS

 This paper was selected as an Editor's Pick



[View Online](#)



[Export Citation](#)



[CrossMark](#)

### ARTICLES YOU MAY BE INTERESTED IN

[Gyrokinetic simulation of turbulence and transport in the SPARC tokamak](#)

Physics of Plasmas **28**, 072502 (2021); <https://doi.org/10.1063/5.0047789>

[Gyrokinetic entropy balances and dynamics in toroidal flux-driven ITG turbulence](#)

Physics of Plasmas **28**, 082304 (2021); <https://doi.org/10.1063/5.0056058>

[Announcement: The 2020 James Clerk Maxwell Prize for Plasma Physics](#)

Physics of Plasmas **28**, 080201 (2021); <https://doi.org/10.1063/5.0063257>

Submit Today!

## Physics of Plasmas

Special Topic: Plasma Physics  
of the Sun in Honor of Eugene Parker



# Analysis of zonal flow pattern formation and the modification of staircase states by electron dynamics in gyrokinetic near marginal turbulence



Cite as: Phys. Plasmas **28**, 072305 (2021); doi: [10.1063/5.0054358](https://doi.org/10.1063/5.0054358)

Submitted: 17 April 2021 · Accepted: 6 July 2021 ·

Published Online: 21 July 2021



[View Online](#)



[Export Citation](#)



[CrossMark](#)

F. Rath,<sup>a)</sup> A. G. Peeters, and A. Weikl

## AFFILIATIONS

University of Bayreuth, Physics Department, 95440 Bayreuth, Germany

<sup>a)</sup>Author to whom correspondence should be addressed: [Florian.Rath1@uni-bayreuth.de](mailto:Florian.Rath1@uni-bayreuth.de)

## ABSTRACT

Microturbulence close to marginality with inclusion of electron dynamics and in the electrostatic limit [A. Weikl *et al.*, Phys. Plasmas **25**, 072305 (2018)] is revisited. In such states the  $E \times B$  shearing rate  $\omega_{E \times B}$ , i.e., the second radial derivative of the zonal electrostatic potential, a quantity often applied to study zonal flow structure formation, has been found to be dominated by radial fine scale features. Those features are significantly different from the mesoscale  $E \times B$  staircase structures [G. Dif-Pradalier *et al.*, Phys. Rev. E **82**, 025401(R) (2010)] normally occurring close to the threshold. Instead of the  $E \times B$  shearing rate, here, zonal flow structure formation is studied through the zonal flow shear induced tilt of turbulent structures, which is measured by director field methods. In contrast to dominant fine scale features in  $\omega_{E \times B}$ , mesoscale zonal flow pattern formation on two disparate scales is identified: (i) A zonal flow with radial scale of the boxsize develops, (ii) superposed by zonal flow corrugations in form of shear layers emerging in the vicinity of lowest order rational layers. This mesoscale zonal flow pattern exhibits properties of  $E \times B$  staircases: (i) A shearing rate of  $\sim 10^{-1} v_{th,i}/R_0$  ( $v_{th,i}$  is the ion thermal velocity and  $R_0$  is the major radius), comparable to typical growth rates, can be attributed to both components of the mesoscale pattern. (ii) Avalanche-like turbulent transport events organize spatially on the same mesoscales. (iii) Shear stabilization by a background  $E \times B$  shear flow requires values of the background shearing rate exceeding those connected to the mesoscale pattern. In conclusion, this work demonstrates that  $E \times B$  staircases do develop, even when the  $E \times B$  shearing rate  $\omega_{E \times B}$  is dominated by radial fine scale features. The  $E \times B$  shearing rate  $\omega_{E \times B}$ , therefore, fails to estimate the shear provided by zonal flows when fine scale structures dominate its radial profile.

© 2021 Author(s). All article content, except where otherwise noted, is licensed under a Creative Commons Attribution (CC BY) license (<http://creativecommons.org/licenses/by/4.0/>). <https://doi.org/10.1063/5.0054358>

## I. INTRODUCTION

A rich body of literature demonstrates the significance of radially sheared zonal flows (ZFs), i.e., toroidally symmetric plasma flows due to the  $E \times B$ -drift, for both the nonlinear saturation<sup>1–4</sup> as well as the nonlinear stabilization<sup>5–8</sup> of microturbulence in tokamak plasmas. The underlying process is mediated by the  $E \times B$  nonlinearity and can be understood either as resulting from the deformation or equivalently tilting of turbulent structures through the advection by the sheared ZFs,<sup>5,9,10</sup> or as a ZF mediated spectral transfer of energy to larger radial wave vectors.<sup>2–4</sup> As a consequence of ZF shearing, turbulent structures exhibit an anisotropy or equivalently a tilt in position space; a property robustly observed in experiments<sup>11–13</sup> and simulations.<sup>1,10</sup>

A metric that characterizes the strength of this shearing process is the  $E \times B$  shearing rate  $\omega_{E \times B}$ , i.e., the radial derivative of the

advecting ZF velocity.<sup>9,14</sup> Shear stabilization of microturbulence is then often expressed in the form of the empirical Waltz rule  $\omega_{E \times B} \sim \gamma$ ,<sup>7,14</sup> where  $\gamma$  denotes the maximum linear growth rate of the underlying microinstabilities. Gyrokinetic studies support this condition.<sup>15,16</sup>

Since the nonlinear threshold for turbulence generation is directly related to shear stabilization,<sup>8</sup> the stabilization rule  $\omega_{E \times B} \sim \gamma$  suggests the shearing rate connected to ZFs close to marginality being of the order of typical growth rates. Indeed, the more recently discovered mesoscale ZF states in near marginal turbulence, also known as  $E \times B$  staircases,<sup>17</sup> exhibit amplitudes in terms of the  $E \times B$  shearing rate satisfying the stabilization criterion remarkably well.<sup>18,19</sup>

The development of mesoscale staircase states is a robust phenomenon close to marginality when electrons are treated adiabatically.<sup>17–21</sup> By contrast, recent gyrokinetic studies that include electron

dynamics report the development of dominant radial fine scale zonal structures.<sup>22–24</sup> Not only is the radial scale of such structures one order of magnitude smaller than the mesoscale of  $E \times B$  staircases, also their  $E \times B$  shearing rate is found to be one order of magnitude larger than typical growth rates.<sup>24</sup> Although the shearing rate connected to fine scale features exceeds typical growth rates significantly, turbulence is not quenched by such ZF structures. Most notably, in contrast to the adiabatic electron case,  $E \times B$ -staircase structures cannot be identified in the radial profile of  $\omega_{E \times B}$  for cyclone base case (CBC) parameters<sup>8</sup> when kinetic electrons are included. Specific parameter choices, i.e., an increased magnetic shear compared to CBC parameters, have been necessary for the re-occurrence of  $E \times B$  staircase structures also in kinetic electron models.<sup>24</sup>

The above observations and discrepancies lead to the following questions: Do zonal fine scale structures prevent the development of mesoscale staircase structures? Why do fine scale features not result in shear stabilization although they over-satisfy the stabilization rule? Questions which will be addressed to in this work.

This work continues on from the work presented in Ref. 24 which uses the  $E \times B$  shearing rate  $\omega_{E \times B}$  for the characterization of ZF pattern formation. Here, however, director field techniques<sup>25</sup> are applied to study zonal flow structure formation; a technique that has found application in the microturbulence context in Ref. 26. This method is based on the ZF induced tilting of turbulent structures and, therefore, represents a more direct way of quantifying the ZF shearing compared to the  $E \times B$  shearing rate. The focus lies on the detection of mesoscale ZF signatures and a comparison with fine scale structures. The remainder is organized as follows: In Sec. II the simulation setup and the director field technique is described. The numerical results are presented in Sec. III, consisting of an investigation of mesoscale zonal potential signatures in Sec. IIIA, the director field analysis in Sec. IIIB and a study of the interplay of staircase states (detected in Sec. IIIC) with background  $E \times B$  shear flows and turbulent heat transport in Sec. IIID. Concluding remarks are given in Sec. IV.

## II. NUMERICAL SETUP AND DIAGNOSTICS

### A. Gyrokinetic simulation setup

Nonlinear gradient-driven gyrokinetic simulations performed with the flux-tube version of Gyrokinetic Workshop (GKW)<sup>27</sup> under the  $\delta f$ -approximation are investigated. The plasma parameters are those of the CYCLONE base case (CBC):<sup>8</sup> inverse aspect ratio  $\epsilon = 0.19$ , safety factor  $q = 1.4$ , magnetic shear  $\hat{s} = 0.78$ , same ion and electron inverse temperature gradient length  $R/L_{Ti} = R/L_{Te} = R/L_T$ , inverse density gradient length  $R/L_n = 2.2$ , equal ion and electron background temperature  $T_i = T_e = T_0$ . No plasma rotation and no collisions are considered. Both a single ion species (deuterium) and electrons are treated as separate kinetic species with an electron to ion mass  $m_e/m_i = 2.72 \times 10^{-4}$ . A small normalized pressure  $\beta = 3 \times 10^{-4}$  is applied to include shear Alfvén wave physics. This allows for larger time steps and reduces the numerical cost. Furthermore, an *ad hoc* circular geometry is chosen. GKW is formulated in field aligned Hamada coordinates<sup>28</sup>  $(\psi, \zeta, s)$ :  $\psi$  labels the flux surfaces and represents the radial coordinate,  $\zeta$  labels the field lines and is an approximate binormal or toroidal coordinate, and  $s$  parameterizes the length along the field lines and represents a poloidal coordinate. The numerical setup, i.e., grid resolution, boundary conditions and numerical

dissipation, is identical to the standard set  $G_2$  of Ref. 24 and for details the reader is referred to the aforementioned reference.

### B. Director field diagnostic

In this work the orientation of tilted turbulent structures is measured by means of the director field.<sup>25</sup> This technique has already been applied to gyrokinetic turbulence in order to detect zonal flow shear zones.<sup>26</sup> Furthermore, measurements of eddy tilting in connection with sheared  $E \times B$  flows also find application in various machines such as DIII-D,<sup>11</sup> Tore Supra,<sup>29</sup> MAST<sup>12</sup> and ASDEX Upgrade.<sup>13</sup>

The director field of a two dimensional field  $G(x, y)$  is defined by

$$k_G = \varphi(\bar{k}_G / |\bar{k}_G|), \quad (1)$$

where

$$\bar{k}_G = \left( \frac{\partial G}{\partial y} \right)^2 - \left( \frac{\partial G}{\partial x} \right)^2 - 2i \frac{\partial G}{\partial y} \frac{\partial G}{\partial x} \quad (2)$$

and  $\varphi$  is the angle of the complex number  $\bar{k}_G / |\bar{k}_G| = A \exp(i\varphi)$  with  $A, \varphi \in \mathbb{R}$ . The director field maps the local orientation of structures in the morphology of  $G$  onto an angle with  $k_G \in [-\pi, +\pi]$ . It is reasonable to define turbulent structures in a 2D field  $G(x, y)$  as structures formed by contour lines. The local tilting angle  $\Theta$  of a turbulent structure may then be defined through the angle formed by the  $x$ -axis and the tangent to the contour line. This allows for a descriptive interpretation of the director field in terms of the tilting angle by noting the relation  $\Theta = k_G/2$  with  $\Theta \in [-\pi/2, +\pi/2]$ . The validity of the tilting angle on the half circle mirrors the invariance of the orientation under rotation by  $\pi$ .

In this work the director field of the turbulent part of the electrostatic potential

$$\tilde{\phi} = \phi(\psi, \zeta, s \approx 0) - \frac{1}{L_\zeta} \int_{-L_\zeta/2}^{L_\zeta/2} d\zeta \phi(\psi, \zeta, s \approx 0) \quad (3)$$

normalized by  $\rho_* T_0/e$  ( $\rho_* = \rho_i/R_0$  is the normalized Larmor radius,  $\rho_i$  is the ion thermal Larmor radius and  $T_0$  is the background temperature) and taken at the low field side (LFS)  $s \approx 0$  is investigated (unless stated otherwise) and, hence,  $x \rightarrow \psi$ ,  $y \rightarrow \zeta$  in Eq. (2). The characterization of turbulent eddies through structures in  $\phi$  at the LFS is justified by both the  $E \times B$ -drift being approximately tangential to contours in  $\tilde{\phi}$ <sup>30</sup> and the turbulence intensity peaking at the LFS. Since the zonal  $E \times B$  flow, and equivalently its shearing rate, is constant in  $\zeta$  per definition, the director field is always averaged over  $\zeta$  which is denoted by  $K_G = \langle k_G \rangle_\zeta$ .

## III. NUMERICAL RESULTS

### A. Investigation of mesoscale zonal potential signatures

In this section an investigation of mesoscale zonal potential signatures in turbulent states close to marginality is presented. The mesoscale is defined by the radial scale of the box size  $L_\psi = 76.27 \rho_i$  and therefore relates to the zonal flow mode number  $n_{ZF} = 1$  (the zonal flow wave vector is  $k_{ZF} = 2\pi n_{ZF}/L_\psi$ ).

#### 1. Temporal long-term evolution

Although the turbulent ion heat flux  $Q_{es,i}$  typically saturates non-linearly within an initial time period of a few  $10^2$  transit times  $R_0/v_{th,i}$ ,

a transition to quasi-stationary stages with reduced flux [e.g., the time interval  $t \in [2250, 3900] R_0/v_{\text{th},i}$  for  $R/L_T = 4.0$  (blue) in the top panel of Fig. 1] occurs at late times for cases close to marginality. Here, the species heat flux is defined by

$$Q_{\text{es,sp}} = \int d^3v \frac{1}{2} m_{\text{sp}} v^2 (\mathbf{v}_E \cdot \nabla \psi) f_{\text{sp}}, \quad (4)$$

where  $m_{\text{sp}}$  is the species mass,  $\nabla \psi \cdot \mathbf{v}_E$  is the radial component of the  $E \times B$  drift and the flux being normalized by  $\rho_*^2 n_0 T_0 v_{\text{th},i}$  with the background density  $n_0$ . The heat flux during both the periods with high and reduced turbulence level is mediated by avalanches (see also Sec. III C 2). The time scales connected to both the point of transition as well as the duration of the quasi-stationary stage can be large, i.e., up to several  $10^3 R_0/v_{\text{th},i}$ , introducing a temporal long-term behavior.

The transition in  $Q_{\text{es,i}}$  is correlated with a temporal long-term evolution of the mesoscale zonal potential component. The saturation of the shear in the  $n_{\text{ZF}} = 1$  zonal mode to its maximum value agrees with the transition in the turbulent level (see mid panel of Fig. 1). Here, the  $E \times B$  shear rate is defined through<sup>18,24,31</sup>

$$\omega_{\text{ExB}} = \frac{1}{2} \frac{\partial^2 \langle \phi \rangle}{\partial \psi^2}, \quad (5)$$

where the zonal electrostatic potential is estimated by

$$\langle \phi \rangle = \frac{1}{L_\zeta} \int_{-L_\zeta/2}^{L_\zeta/2} d\zeta \phi(\psi, \zeta, s \approx 0). \quad (6)$$

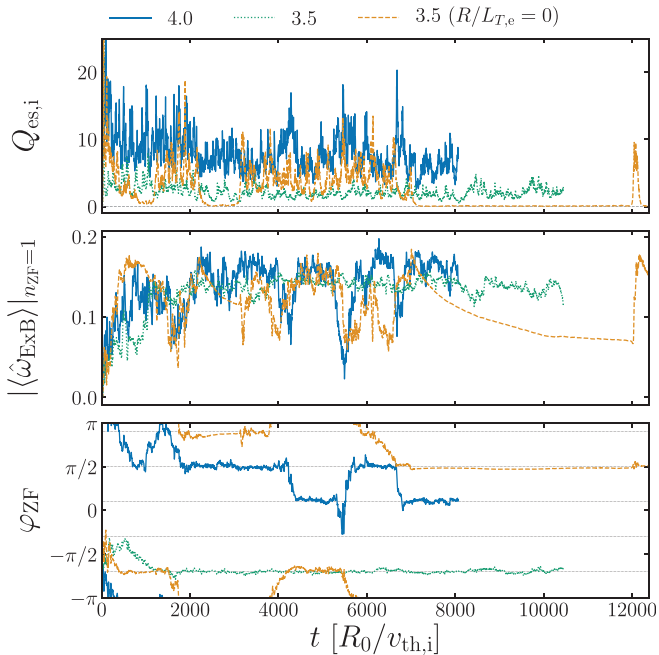


**FIG. 1.** Time trace of the volume averaged ion electrostatic heat flux  $Q_{\text{es,i}}$  (top), the shear carried by the  $n_{\text{ZF}} = 1$  zonal mode  $|\langle \omega_{\text{ExB}} \rangle|_{n_{\text{ZF}}=1}$  in terms of  $v_{\text{th},i}/R_0$  (mid) and its radial phase  $\varphi_{\text{ZF}}$  in terms of radians (bottom) for cases with  $R/L_{T_i} = R/L_{T_e} = 4.0$  (blue, solid),  $R/L_{T_i} = R/L_{T_e} = 3.5$  (green, dotted) and  $R/L_{T_i} = 3.5$  and  $R/L_{T_e} = 0$  (orange, dashed). Mind the periodicity of  $\varphi_{\text{ZF}}$  on  $[-\pi, \pi]$ .

The mesoscale shear  $|\langle \omega_{\text{ExB}} \rangle|_{n_{\text{ZF}}=1}$  is defined by the Fourier coefficient connected to the zonal flow wave vector  $k_{\text{ZF}} = 2\pi n_{\text{ZF}}/L_\psi$  with  $n_{\text{ZF}} = 1$  and is obtained by a radial Fourier transform of the zonal flow shearing rate. Estimated times scales on which the  $n_{\text{ZF}} = 1$  zonal mode saturates to its quasi-stationary maximum value vary between several  $10^2$ – $10^3 R_0/v_{\text{th},i}$  and show no systematic dependence on  $R/L_T$ . The observed long-term behavior requires a long time integration to accurately describe the turbulent transport levels, since a reduction of 28%–37% can occur as summarized in Table I. The existence of this long-term behavior is not always appreciated in literature.

A similar temporal long-term behavior close to the nonlinear threshold is typically observed in studies that apply the adiabatic electron closure. In those cases a staircase state develops, quenching the turbulence after considerable time scales up to  $10^3$ – $10^4 R_0/v_{\text{th},i}$ . The result is a non-monotonic dependence of the heat flux on  $R/L_T$ , referred to as the finite heat flux threshold,<sup>19</sup> which expresses the inability of the local gradient-driven approach (with adiabatic electrons) to correctly access near marginal turbulence. It is therefore justified to ask whether (i) the present simulations are temporally converged and (ii) the local gradient-driven approach is appropriate to access near marginal turbulence.

In the present simulations with kinetic electrons and CBC parameters a transition from finite turbulence to suppressed states similar to Ref. 19 has not been observed. As reported in the aforementioned reference the onset of this transition is parameter dependent and occurs at earlier times with reduction of  $R/L_T$ . Although the case with  $R/L_T = 3.5$  has been run up to 10 000  $R_0/v_{\text{th},i}$  (see green dotted data in Fig. 1) no significant time evolution of both the turbulence and mesoscale shear level can be observed in the long time limit. The present simulations are, hence, considered temporally converged.

The flux-gradient relation (see Fig. 4) shows a smooth transition to turbulence, demonstrating that the local gradient-driven approach with kinetic electrons is able to access near marginal turbulence with arbitrary heat flux levels (at least for the plasma parameters compliant to the data shown). Indeed, the inclusion of electron physics results in a different overall turbulence regime. In order to elucidate this statement further a case with  $R/L_{T_i} = 3.5$  but  $R/L_{T_e} = 0$  has been investigated (see orange dashed data in Fig. 1). This case features turbulence—mesoscale zonal flow dynamics similar to gradient-driven simulations with the adiabatic electron approximation just below the finite heat flux threshold;<sup>19</sup> transitions between extended phases with finite intermittent turbulence and suppressed states are clearly visible. This outcome indicates that the ability of the local gradient-driven approach (with kinetic electrons and CBC parameters) in accessing arbitrary near marginal turbulent states is related to electron instabilities that are not included into an adiabatic electron description. Due to this outcome the local gradient-driven approach with kinetic

**TABLE I.** Temporally and volume averaged ion electrostatic heat flux  $Q_{\text{es,i}}$  (in terms of  $\rho_*^2 n_0 T_0 v_{\text{th},i}$ ) during high turbulent states  $\Delta T_1$  and reduced turbulent states  $\Delta T_2$  after the transition (both time intervals in terms of  $R_0/v_{\text{th},i}$ ) for two cases which exhibit clearly separated turbulent periods.

$R/L_T$	$\Delta T_1$	$\Delta T_2$	$Q_{\text{es,i}} _{\Delta T_1}$	$Q_{\text{es,i}} _{\Delta T_2}$
4.0	225–1800	2250–3900	9.48	6.80
3.5	75–2025	3825–6979.5	3.09	1.93

electrons is valued an appropriate (and computationally feasible) approach to access near marginal turbulence.

## 2. Radial lock-in of mesoscale structures

The long-term evolution of the mesoscale zonal potential mode exhibit a concomitant reduction in its radial variability. Here, the radial orientation is diagnosed through the use of the radial phase  $\varphi_{ZF}$  defined by

$$\hat{\omega}_{E \times B}(k_{ZF}) = \hat{\omega}_{E \times B}^A(k_{ZF}) \exp[i\varphi_{ZF}(k_{ZF})] \quad (7)$$

with  $\hat{\omega}_{E \times B}^A, \varphi_{ZF} \in \mathbb{R}$  and  $\hat{\omega}_{E \times B}$  being the complex Fourier coefficient of the  $E \times B$  shear [Eq. (5)] connected to the ZF mode with wave vector  $k_{ZF}$ . A striking observation is the lock-in of the longest wavelength zonal mode at distinct radial locations. This mode keeps its radial orientation for long time periods as indicated by the restriction of  $\varphi_{ZF}$  to specific values highlighted by horizontal dotted lines in the bottom panel of Fig. 1. Extended phases with lock-in behavior are dispersed by intermittent phases with increased turbulent level, reduced mesoscale zonal potential level and elevated radial variability. The latter allows for the radial migration of the mesoscale zonal potential component pattern among different lock-in positions.

This outcome holds for a wider range in  $R/L_T$  as shown by the temporal distribution of the radial phase PDF( $\varphi_{ZF}$ ) normalized to the maximum of the respective distribution (see Fig. 2). An  $i_k$ -fold symmetry is found, where  $i_k = 5$  specifies the number of lowest order rational layers (LORLs) in the simulation domain. LORLs are radial locations with high symmetry, in that all  $k_\zeta$ -modes project onto itself when connected over the radial boundary leading to strict parallel periodicity, and are determined by the geometry of the confining magnetic field. The radial lock-in behavior, therefore, demonstrates an

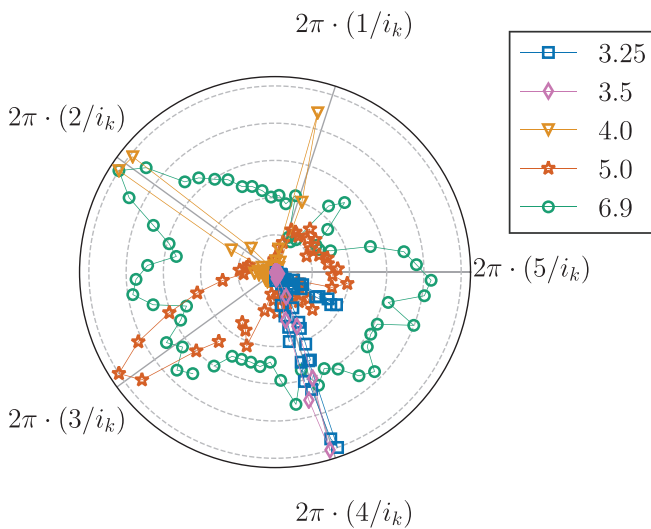


**FIG. 2.** Distribution of the radial phase  $\varphi_{ZF}$  of the  $n_{ZF} = 1$  mode in the  $E \times B$  shear [Eq. (7)] with respect to its domain of validity  $\varphi_{ZF} \in [0, 2\pi[$  (full circle) during the stationary state for various realizations of  $R/L_T$ . The five ( $i_k = 5$ ) radial gray rays depict the orientations to which the  $n_{ZF} = 1$  zonal mode locks in (compare bottom panel of Fig. 1). The individual distributions are normalized to the respective maximum.

interplay of mesoscale zonal potential structures with lowest order rational surfaces. Furthermore, the radial variability increases with  $R/L_T$ . While the radial orientation in cases with  $R/L_T \in [3.25, 3.5, 4.0]$  is strongly tied to LORLs, the radial phase distribution indicates an increased mobility around LORLs for  $R/L_T = 5.0$  and an almost random phase distribution at  $R/L_T = 6.9$ .

## 3. Spatial scale dependence of the $E \times B$ shear

Here, a quantitative analysis of the  $E \times B$  shearing rate connected to meso- and fine scale zonal structures is provided. The shear carried by the mesoscale zonal potential component  $|\langle \hat{\omega}_{E \times B} \rangle|_{n_{ZF}=1}$  (red “+” in Fig. 3) is a further characteristic of the above-mentioned late quasi-stationary states. In general, the mesoscale shear level is of the order of  $10^{-1} v_{th,i}/R_0$  and, hence, agrees with typical values of the growth rate as well as staircase amplitudes.<sup>18,19</sup> A striking observation is the linear increase in the interval  $R/L_T = 2.9–3.5$  following the rule  $\omega_{E \times B} \sim \gamma$ . For inverse temperature gradient lengths around  $R/L_T = 3.5$  the mesoscale ZF level is limited to an amplitude of  $\omega_{E \times B} \approx 0.15 v_{th,i}/R_0$ . Narrow quartiles indicate the temporal persistence of this typical mesoscale level, which is confirmed by the time traces in Fig. 1. Further increase in  $R/L_T$  results in a slight decrease in the averaged mesoscale ZF level. And although the temporal distribution is somewhat broadened the upper and lower quartiles show that 75% of the time the ZF state still resides at amplitudes of  $\hat{\omega}_{E \times B} \sim 0.1–0.15 v_{th,i}/R_0$ . In Ref. 21 similar observations have been made in connection to  $E \times B$  staircase states.

The above discussed characteristics of the mesoscales have to be contrasted to the shear carried by fine scale features (blue “×” in Fig. 3) that significantly exceeds the shear carried by the mesoscale component. Here, an estimate of the amplitude of fine scale features is provided by the spike intensity

$$\Delta\omega_{E \times B} = \frac{1}{N_{\text{spikes}}} \sum_{i=1}^{N_{\text{spikes}}} |\omega_{E \times B}(\psi_i)|, \quad (8)$$

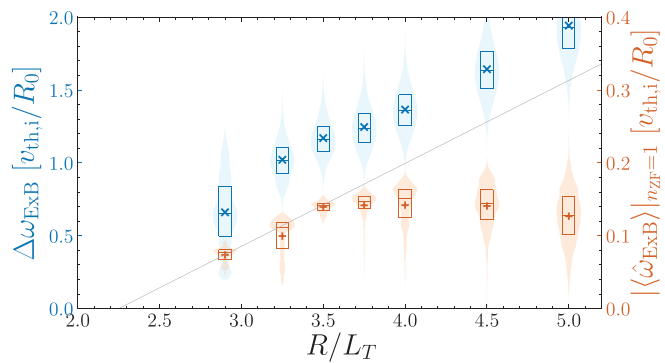


**FIG. 3.** Temporally averaged spike intensity in the  $E \times B$  shearing rate  $\Delta\omega_{E \times B}$  (blue ×, left axis) and shear carried by the mesoscale  $n_{ZF} = 1$  zonal flow mode  $|\langle \hat{\omega}_{E \times B} \rangle|_{n_{ZF}=1}$  (red +, right axis) against  $R/L_T$ . Shaded regions represent the temporal distribution and boxes indicate the upper and lower quartiles. The growth rate of the most unstable mode is depicted by a thin gray line (with respect to right axis).

where  $\omega_{E \times B}(\psi_i)$  is the shearing rate taken at the radial position of a spike  $\psi_i$  and  $N_{\text{spikes}}$  denotes the number of spikes in the radial profile of  $\omega_{E \times B}$  at a fixed point of time. A spike is defined by a local extremum in the radial profile of  $\omega_{E \times B}$  (blue profiles in Fig. 6). In contrast to the averaged mesoscale shear, the averaged spike intensity increases monotonically with  $R/L_T$ .

Both the large spike intensity and the linear increase is in contradiction with the obtained turbulent level (see Fig. 4) when the Waltz stabilization rule  $\gamma \sim \omega_{E \times B}$  is considered. The dependence of the shear carried by mesoscale zonal potential structures, however, appears to be consistent with the increase in the turbulent level for  $R/L_T > 3.5$ . This suggests that the fine scale features in  $\omega_{E \times B}$  are less relevant for the shear stabilization of turbulence.

## B. Director field analysis

In this section the director field diagnostic introduced in Sec. II B is applied in order to investigate ZF pattern formation through the shear induced tilting of turbulent structures.

### 1. Director field in the presence of a homogeneously sheared background $E \times B$ flow

Before the director field method is applied to turbulence generated radially periodic ZFs, here, the connection between the  $E \times B$  flow shearing rate and the director field is established using a constant (both in time and space) sheared background  $E \times B$  flow.

The background shear flow is introduced through the additional convective term

$$\frac{\partial g}{\partial t} + -\mathbf{v}_s \cdot \nabla g - \rho_*^2 \frac{\partial \bar{\Phi}}{\partial \psi} \mathcal{E}^{\psi\zeta} \frac{\partial g}{\partial \zeta} = -2\gamma_E \psi \mathcal{E}^{\psi\zeta} \frac{\partial g}{\partial \zeta} \quad (9)$$

on the right hand side of the GK equation. The constant background  $E \times B$  shearing rate is defined by

$$\gamma_E = \frac{1}{2} \rho_*^2 \frac{\partial^2 \bar{\Phi}}{\partial \psi^2}, \quad (10)$$

where  $\bar{\Phi}$  is the electrostatic potential connected to the sheared background  $E \times B$  drift and  $\mathcal{E}^{\psi\zeta}$  a related geometry tensor.<sup>27</sup> In GK the background shear is implemented using the wave vector remapping method of Ref. 32 that has been benchmarked in Ref. 16.

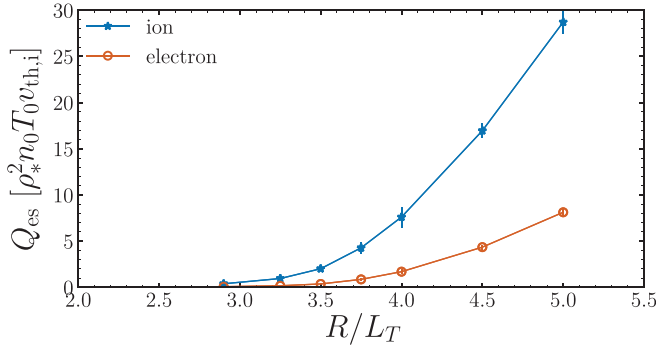


FIG. 4. Time and volume averaged electrostatic heat flux  $Q_{es}$  of ions (blue) and electrons (red) against the background inverse temperature gradient length.

Without external sources of shear as well as persistent ZFs symmetry properties of the gyrokinetic equation require the turbulent structures at the LFS ( $s=0$ ) to be radially symmetric in a statistically sense.<sup>12</sup> As a consequence, the ensemble averaged local orientation of turbulent structures and, hence, the director field have to vanish. However, even in the presence of periodic ZFs the director field can be made to vanish when averaging over the radial direction, since negative and positive shear zones cancel. Eddies that experience an  $E \times B$  shear being constant over the simulation domain, in turn, exhibit a preferential tilt. The radially averaged director field  $\langle K_\phi \rangle_\psi$  ( $\langle \dots \rangle_\psi$  denotes a radial average) is then finite and is, therefore, measured in the analysis below. Due to the even number of grid points along the field line ( $N_s = 32$ ) and the finite magnetic shear  $\hat{s}$  of the chosen numerical parameters the 2D slice of the potential  $\bar{\phi}(\psi, \zeta, s \approx 0)$  used in the director field diagnostic is slightly off the LFS. This results in a small radially constant positive tilt of turbulent eddies due to the alignment of turbulent modes along the sheared magnetic field.<sup>33</sup> It has been verified that an odd number of  $s$ -grid points, and consequently the positioning of the potential slice at  $s=0$ , removes this offset. In order to mitigate this effect, the radially averaged director field at arbitrary background shear  $\langle K_\phi \rangle_\psi$  is corrected by the radially averaged director field at zero shear  $\langle K_\phi \rangle_\psi|_{\gamma_E=0}$ , i.e.,  $\langle K_\phi \rangle_\psi - \langle K_\phi \rangle_\psi|_{\gamma_E=0}$ , at fixed value of  $R/L_T$ . It has been ensured that the radially averaged director field at finite background shear is always significantly larger than the radially averaged director field at zero shear (the latter is summarized in Table II).

Since already a small level of background shear is known to result in complete stabilization in the linear regime,<sup>14,34</sup> late nonlinearly saturated states without background shear are used as initial conditions for realizations with finite background shear. This procedure is required to access stationary turbulent states at finite background shear. Furthermore, only cases with well defined, i.e., non-quenched, turbulence are considered, since it will be evident below that the director field depends on the turbulent level.

In general, the averaged director field and, hence, the level of eddy tilt increases with the background shear (see Fig. 5) as expected.<sup>12</sup> The sign sensitivity has been ensured through a sample point with  $R/L_T = 6.9$  and  $\gamma_E = -0.1$  (not shown) which results in a negative averaged director field. Figure 5 makes clear that the mapping between the shearing rate  $\gamma_E$  and the director field  $\langle K_\phi \rangle_\psi$  is not unique. An increase in  $R/L_T$  and therefore the turbulence level (see also Fig. 12) at same level of background shear results in a reduction of the averaged director field and equivalently the averaged tilt of eddies. This observation is partly interpreted as a reduction of the eddy lifetime, i.e., the time during which turbulent structures can be tilted by the sheared  $E \times B$  flow, with increasing turbulence level.<sup>12</sup> Furthermore, the velocity shear connected to turbulent structures itself, i.e., turbulent mixing, might compete the background  $E \times B$  shear with increasing turbulence

TABLE II. Radially and time averaged director field without background shear  $\langle K_\phi \rangle_\psi|_{\gamma_E=0}$  and fit parameter  $\alpha_{\text{cal}}$  of the linear model Eq. (11) corresponding to individual  $R/L_T$ -realizations in Fig. 5.

$R/L_T$	3.5	4.0	5.0	6.9
$\langle K_\phi \rangle_\psi _{\gamma_E=0}$ (rad)	0.009	0.047	0.055	0.118
$\alpha_{\text{cal}}$ [rad $\cdot R_0/v_{th,i}$ ]	9.25	8.21	7.70	4.80

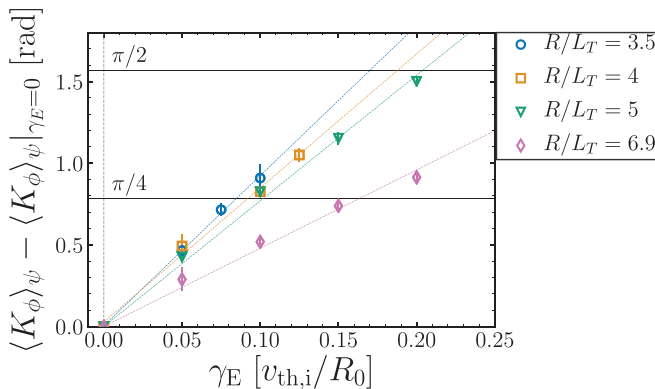


**FIG. 5.** Temporally and radially averaged corrected director field  $\langle K_\phi \rangle_\psi - \langle K_\phi \rangle_{\psi=0}$  against the background  $E \times B$  shearing rate  $\gamma_E$  for various values of the inverse background temperature gradient length. Only stationary turbulent states are depicted and dashed lines represent fits of the model Eq. (11).

strength and thereby lead to an isotropization as the  $E \times B$  nonlinearity tend to produce isotropic eddies.<sup>30</sup> It is noted, however, that this dependency poses no problem for the director field analysis of turbulence generated zonal flows in Secs. III B 2–III B 5, since a fixed value of  $R/L_T$  ensures a roughly constant turbulence level during the stationary state (see top panel of Fig. 3).

Given the complex interplay of sheared ZFs and turbulence, the development of a general model describing the averaged director field response on the  $E \times B$  shearing rate is not further investigated here. Motivated by the outcome shown in Fig. 5 and for simplicity a linear dependence

$$K_\phi = \alpha_{\text{cal}} \gamma_E \quad (11)$$

is adopted with the constant  $\alpha_{\text{cal}}$  having the unit  $\text{rad} \cdot R_0/v_{\text{th},i}$ . The linear model applies satisfactory well (dashed lines in Fig. 5) within the considered range of  $\gamma_E$  and provides a proxy for the conversion of the averaged director field into an  $E \times B$  shearing rate. The corresponding fit parameter  $\alpha_{\text{cal}}$  is summarized in Table II.

To conclude, this numerical experiment demonstrates that the level of eddy tilt ( $\sim K_\phi$ ) provides information about the zonal flow induced shear ( $\sim \gamma_E$ ). This motivates the application of director field techniques for the investigation of the shearing action provided by turbulence generated sheared zonal flows below.

## 2. Director field analysis of turbulence generated radially periodic zonal flows

In this section the director field method is applied to investigate the deformation of turbulent structures induced by self-consistently generated radially periodic ZFs. None of the simulations presented here and in the remainder of Sec. III B apply background  $E \times B$  shear, such that the considered sheared ZFs evolve self-consistently, i.e., with back-reaction to the turbulence. In order to separate the deformation induced by radially periodic ZFs from the constant tilt due to the alignment along the sheared background magnetic field (see also Sec. III B 1), the radially averaged director field  $\langle K_G \rangle_\psi$  is always subtracted from the total director field  $K_G$  in the remainder of Sec. III B. The focus lies on the role of fine- and mesoscale ZFs for the shear induced tilting.

The case selection in this analysis is representative for three distinct regimes with respect to mesoscale  $n_{\text{ZF}} = 1$  structure development in  $\omega_{E \times B}$  (see Fig. 3) as well as turbulent transport level (see Fig. 4): Case (A) with  $R/L_T = 3.25$  lies in the regime with linearly increasing shear in the mesoscale ZF and exhibits a small turbulence level. Case (B) with  $R/L_T = 4.0$  represents the transition to a linearly and more strongly increasing heat flux and is situated in the regime with saturated mesoscale ZF shear. Case (C) with  $R/L_T = 6.9$  is a strong turbulent reference case with highly variable mesoscale ZF (see Fig. 2) at a level of  $\langle |\langle \hat{\omega}_{E \times B} \rangle|_{n_{\text{ZF}}=1} \rangle_t = 0.11 v_{\text{th},i}/R_0$  and high turbulent level  $\langle \langle Q_{\text{es}} \rangle_\psi \rangle_t = 74.33 \rho_*^2 n_0 T_0 v_{\text{th},i}$ .

Evidence of fine scale features in the radial profiles of  $K_\phi$  can only be observed in case (A) (red profile in top left panel of Fig. 6). The level of fine scale features in the director field, however, does not reflect the respective structures in  $\omega_{E \times B}$  (blue profile). While the profile of the shearing rate  $\omega_{E \times B}$  is clearly dominated by fine scale features, it is the  $n_{\text{ZF}} = 1$  mesoscale variation that prevails over the fine scale features in the director field. The actual shearing action, i.e., the ability of tilting turbulent structures, of spikes in  $\omega_{E \times B}$ , hence, appears to be significantly reduced. This observation is in agreement with structures in the spatial morphology of the turbulent electrostatic potential  $\tilde{\phi}$  (bottom left panel of Fig. 6). Therein, the tilting by fine scale features is only faintly visible by radially periodic vertically coherent zigzag structures (see bottom left panel of Fig. 6).

In cases with increasing turbulent level, i.e., case (B) and (C), the fine scale signatures in the director field disappear (mid and right top panels of Fig. 6). This stands in contrast to the increase in the spike intensity in the shearing rate  $\omega_{E \times B}$  (see also  $\Delta\omega_{E \times B}$  in Fig. 3) and is therefore conjectured to be directly related to the increasing turbulence level. Note that both the turbulence correlation length and the scale on which turbulence spreading acts is of the order of several Larmor radii.<sup>35</sup> The zonal flow shear induced tilting on scales of the spike structures is therefore, in particular, susceptible to turbulent mixing. The above observation is confirmed by the absence of vertically aligned zigzag structures and the appearance of small scale and more irregular eddies for  $R/L_T = 4.0$  and  $R/L_T = 6.9$  (mid and right bottom panels of Fig. 6). To conclude, despite the large amplitude ( $\sim 1 v_{\text{th},i}/R_0$ ) of fine scale features in  $\omega_{E \times B}$  their contribution to shear deformation of turbulent structures is marginal in the cases considered here.

A striking observation is the development of mesoscale pattern in the director field (top panels of Fig. 6), occurring on two distinct disparate scales:

- (i) Close to LORLs (vertical black dotted lines) the radial profile of  $K_\phi$  features corrugations. Radial intervals with  $\partial_\psi K_\phi < 0$  are always centered at LORLs introducing an  $i_k$ -fold mesoscale pattern in  $K_\phi$ . It has been verified that this period length changes accordingly with varying  $i_k$ . In case (B) the corrugations result in zero crossings and reduced averaged deformation in the vicinity of LORLs. In the strong turbulent reference case (C) signatures of the  $n_{\text{ZF}} = 1$  mesoscale ZF average out due to its quasi-random phase distribution (see Fig. 2), leaving signatures of the corrugations visible in form of bipolar shear layers centered at LORLs. These spatially fixed corrugations feature amplitudes of  $K_\phi \sim \pi/4$  that can be related to a shearing rate of  $\gamma_E \sim 0.15 v_{\text{th},i}/R_0$  (see Fig. 5). The formation of zonal flow

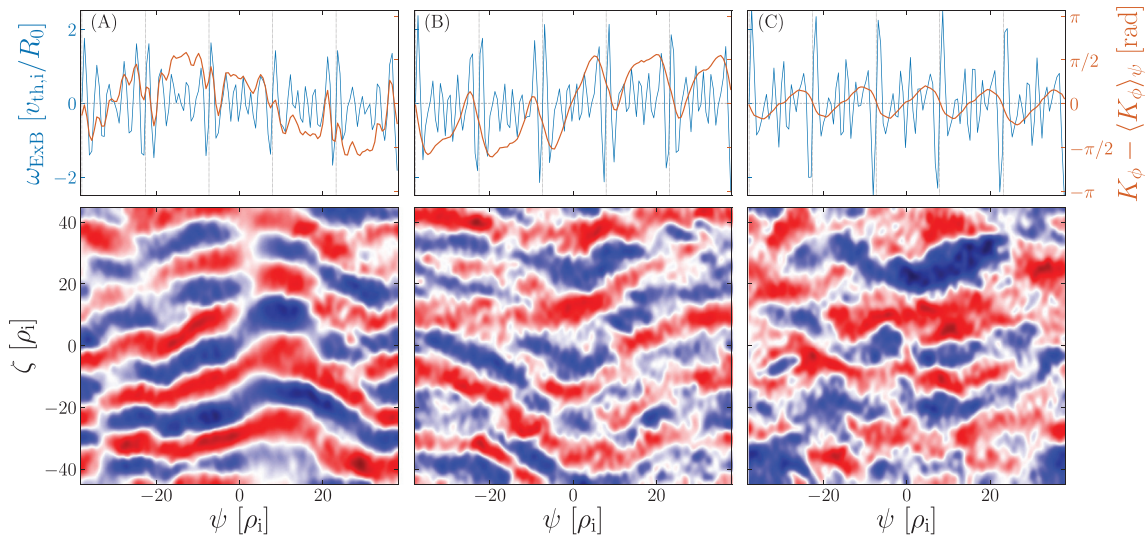


**FIG. 6.** Top panels: Radial profiles of the temporally averaged shearing rate  $\omega_{ExB}$  (blue, left vertical axis) and the director field  $K_\phi - \langle K_\phi \rangle_\psi$  (red, right vertical axis) for cases (A), (B) and (C) described in the text. Vertical black dotted lines indicate LORLs. Bottom panels: Snapshots of the turbulent part of the electrostatic potential  $\tilde{\phi}$  in the  $\psi$ - $\zeta$ -plane at the LFS. The data are taken from the same time intervals used for time averaging of the respective radial profile in the top panels. Bicubic interpolation is applied to enhance the visibility of structures on grid scale. The potential is normalized to its maximum value and the color scale ranges linearly  $\in [-1.05, +1.05] \rightarrow [\text{blue}, \text{red}]$ .

corrugations emerging at low order rational surfaces has been reported in Ref. 36 and is distinct from the fine scale features in  $\omega_{ExB}$  that are not restricted to LORLs.<sup>24</sup>

(ii) The subset of cases with radial lock-in of the mesoscale zonal mode, i.e.,  $R/L_T \in [3.25, 3.5, 3.75, 4.0]$ , exhibits a  $n_{ZF} = 1$  mesoscale variation in the director field when averaging over a locked-in phase. The spatial morphology of turbulent structures confirms the significance of this mesoscale structure in the ZF induced tilting (left and mid bottom panels of Fig. 6). The zero crossing of the  $n_{ZF} = 1$  modulation satisfying  $K_\phi < 0 \rightarrow K_\phi > 0$  with increasing radial coordinate is always centered in between two LORLs, while the opposite zero crossing always coincides with a LORL. It has been verified that this behavior translates to even values of  $i_k$ . As a result, an uneven number of LORLs allows for an even radial symmetry of the structure in  $K_\phi$ . This restriction on the mesoscale pattern is a manifestation of the interplay of the  $n_{ZF} = 1$  ZF component with LOLRs as observed in Sec. III A 2. In case (B) the director field exhibits intervals with finite and almost constant eddy tilt in between the corrugations, indicating a finite shearing rate there. The overall shape resembles a fully-developed staircase<sup>19,21</sup> (this nomenclature follows the aforementioned references and denotes the staircase state emerging in gradient-driven simulations with adiabatic electrons just below the non-monotonic finite heat flux threshold) with the modification of  $i_k - 1$  additional corrugations close to LORLs. Since the development of the corrugations in the present study requires electron dynamics the overall structure will be referred to as a modified staircase state hereafter. Structures of this type occur for  $R/L_T \in [3.5, 3.75, 4.5, 5.0]$  as well (a case with  $R/L_T = 3.5$  is shown in the top left panel of Fig. 7). In the latter two cases the spatial persistence is significantly reduced, which is consistent with a higher radial variability of the largest scale zonal flow

mode (see Fig. 2). The amplitudes of modified staircases of  $K_\phi \sim \pi/2$  can be roughly related to shearing rates of  $\gamma_E \sim 0.15 - 0.2 v_{th,i}/R_0$  through extrapolation of  $K_\phi(\gamma_E)$  obtained in the director field calibration (Fig. 5). It is, therefore,

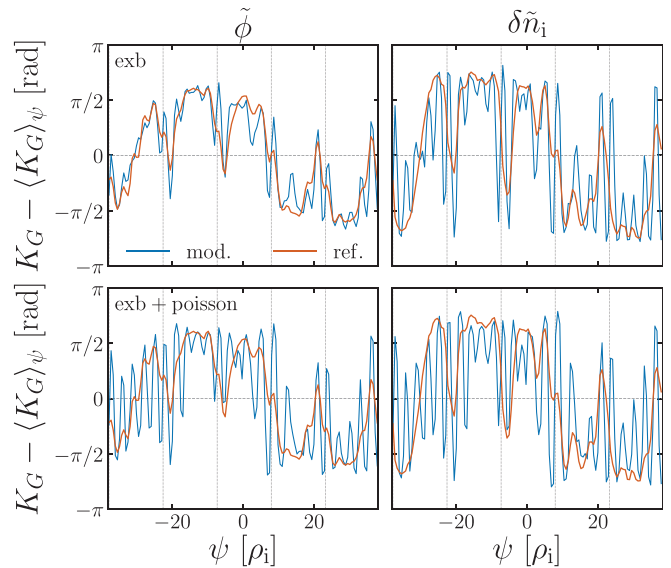


**FIG. 7.** Radial profiles of the temporally averaged director field  $K_G - \langle K_G \rangle_\psi$  of the electrostatic potential  $G = \tilde{\phi}$  (left panels), the ion gyro-center density  $G = \delta\tilde{n}_i$  (right panels). Shown are an unmodified reference case (red) and cases without GA in the  $E \times B$  nonlinearity (blue top panels) as well as without GA in both the  $E \times B$  nonlinearity as well as the integral part of the Poisson equation (blue bottom panels). All cases have  $R/L_T = 3.5$  and vertical black dotted lines indicate LORLs.

comparable to the shear carried by the mesoscale component of zonal potential (see Fig. 3).

The above observations are somewhat surprising and deserve further clarifications. Especially the following questions are raised: (i) Why do the fine scale features in  $\omega_{E \times B}$  hardly contribute to the tilting of turbulent structures? (ii) Can the modified staircase pattern in the director field, and especially the corrugations, be related to physically meaningful perturbations in the distribution function? (iii) Do modified staircase share similarities with their adiabatic counterpart? These questions will be addressed in Secs. III B 3–III B 5 and Sec. III C.

### 3. Role of finite Larmor radius effects for the shearing action of fine scale structures in the shearing rate $\omega_{E \times B}$

A fundamental aspect of the gyrokinetic framework is the dynamical reduction through the average over the fast gyro-motion. The so introduced gyro-average (GA) appears at various places as, for example, in form of the gyro-averaged potential entering the  $E \times B$  nonlinearity of the gyrokinetic equation, or the gyro-averaged distribution function entering the integral part of the Poisson equation.<sup>27</sup> While the gyro-average can be neglected on scales significantly larger than the Larmor radius, it is relevant on scales comparable to it and introduces so-called finite Larmor radius (FLR) effects. The shearing of turbulent structures by zonal  $E \times B$  flow is mediated by the  $E \times B$  nonlinearity and due to the small radial scale of the spike structures of a few Larmor radii (see Fig. 6), their shearing action might be susceptible to FLR effects, in particular.

In order to test if FLR effects mitigate the shearing through small scale features in  $\omega_{E \times B}$ , the gyrokinetic as well as the Poisson equation are manipulated in two steps. First, the gyro-average is neglected in the  $E \times B$  nonlinearity in case it acts on the  $k_\zeta = 0$  mode of the electrostatic potential. This is realized by the modification

$$J_0 \hat{\phi}|_{k_\zeta=0} \rightarrow \hat{\phi}|_{k_\zeta=0} \quad (12)$$

with  $J_0$  being the zeroth order Bessel function and  $\hat{\phi}$  being the Fourier transformed electrostatic potential.

A well saturated base case with  $R/L_T = 3.5$  is used as initial condition for the cases considered below. The base case is restarted both with and without the GA in the  $E \times B$  nonlinearity and the influence on the deformation of turbulent structures in the electrostatic potential  $\tilde{\phi}$  and the ion gyro-center density  $\delta\tilde{n}_i = \delta n_i - \langle \delta n_i \rangle$ , with

$$\delta n_{sp} = \int d^3 v f_{sp}, \quad (13)$$

is characterized by the respective temporally averaged director field (top panels of Fig. 7). Clear fine scale features can be observed in the director field of the ion gyro-center density when the GA is removed (blue) in contrast to the unmodified reference case (red). The spike intensity in the shearing rate  $\omega_{E \times B}$  is not found to be influenced by this modification. This demonstrates that FLR effects mitigate the shearing action of fine scale structures in the shearing rate  $\omega_{E \times B}$  efficiently by filtering fine scale features in the zonal electrostatic potential.

Although the removal of the GA in the  $E \times B$  nonlinearity has profound influences on the ion gyro-center density, its influence on the deformation of turbulent structures in the electrostatic potential is

found to be less pronounced (top left panel). The above outcome is confirmed by the spatial morphology of turbulent structures in the electrostatic potential and gyro-center density (top panels of Fig. 8). Now, clear vertically coherent small scale deformations are visible in the turbulent gyro-center density field (right), while being considerably fainter in the electrostatic potential (left).

The discrepancy relates to polarization effects entering the gyrokinetic Poisson equation due to the pull-back transformation from gyro-center to particle phase space.<sup>37</sup> This involves a further GA in the integral part of Poisson equation<sup>27</sup> and, hence, introduces a second smoothing of small scale features, now, however, of the turbulent structures itself. In order to clarify the above effect, the GA in the integral part of the Poisson equation is neglected when acting on turbulent  $k_\zeta \neq 0$  modes of the distribution function. This second manipulation is realized by the substitution

$$\int J_0 \hat{g}|_{k_\zeta \neq 0} d\mu dv_\parallel \rightarrow \int \hat{g}|_{k_\zeta \neq 0} d\mu dv_\parallel \quad (14)$$

in the integral part of Poisson equation [see Eq. (73) of Ref. 27]. As a result similar profiles of  $K_\phi$  and  $K_{\delta n_i}$  are obtained with  $K_\phi$  now exhibiting spike features as well (bottom panels of Fig. 8). It is noted, that the structures in  $K_\phi$  do not show the same strong spikes as occurring in  $\omega_{E \times B}$  around LORLs (see top panels of Fig. 6). This fact is attributed to the extreme values of the shear at these points for which the validity of the linear model anticipated in Sec. III B 1 cannot be guaranteed. Clear signatures of sheared fine scale structures are now visible also in the spatial morphology of  $\tilde{\phi}$  (bottom panel of Fig. 8). This numerical experiment, hence, demonstrates a significant reduction of the

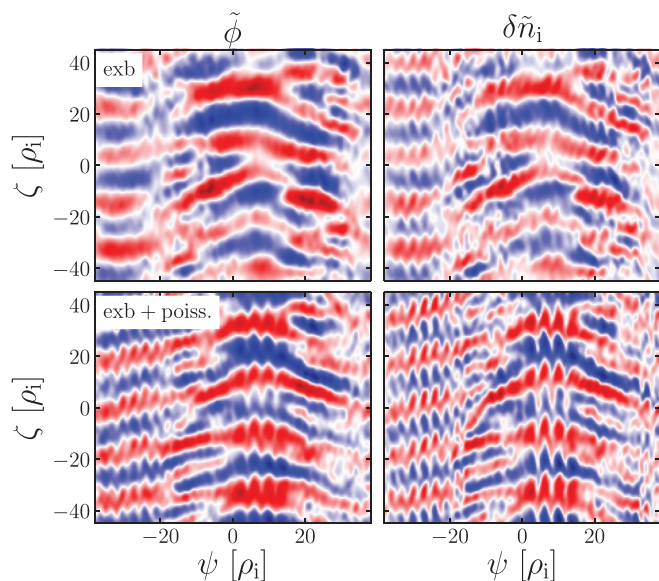


**FIG. 8.** Turbulent part of the electrostatic potential  $\tilde{\phi}$  (left) and the ion gyro-center density (right) in the  $\psi$ - $\zeta$ -plane with the gyro-average removed in the  $E \times B$  nonlinearity (top) and both the  $E \times B$  nonlinearity as well as the integral part of the Poisson equation (bottom). All cases have  $R/L_T = 3.5$ . Bicubic interpolation is applied to enhance the visibility of structures on grid scale. Both quantities are normalized to the maximum value and the color scale ranges linearly  $\in [-1.05, +1.05] \rightarrow [\text{blue, red}]$ .

shearing action connected to fine scale structures in  $\omega_{E \times B}$  due to FLR effects.

While the role of FLR effects for the deformation of turbulent structures has been considered before, now its influence on shear stabilization<sup>5–7</sup> is investigated. Figure 9 shows time traces of the ion and electron electrostatic heat flux for the same cases discussed above. Both manipulations of the gyrokinetic set of equations result in a reduction of the turbulent transport level. In the case without the GA in both the zonal  $E \times B$  nonlinearity as well as the integral part of Poisson equation an extended phase with almost zero heat flux is observed. The spike features in the shearing rate  $\omega_{E \times B}$ , therefore, have the potential to stabilize turbulence through decorrelation. In practice, FLR effects on ion Larmor radius scales render this potential ineffective.

#### 4. Connection of zonal flow corrugations to perpendicular ion pressure corrugations

In this section the corrugations in the director field close to LORLs (see Fig. 6) are related to perpendicular ion pressure corrugations making use of both the parallel electron and the radial ion force balance. Below, only toroidally constant quantities, i.e.,  $k_\zeta = 0$  components, are considered.

Neglecting the electron inertia term and the gyroviscous pressure tensor the parallel electron force balance in lowest order of  $\rho_*$  can be formulated by (see the Appendix)

$$0 = \nabla_{\parallel} \phi - [\mathcal{K}_{\parallel}(p_{\parallel,e}, p_{\perp,e}) + \nabla_{\parallel} p_{\parallel,e}], \quad (15)$$

where  $\nabla_{\parallel} = \mathbf{b} \cdot \nabla$  is the gradient along the magnetic field,  $\mathcal{K}_{\parallel}$  expresses magnetic curvature effects entering through the divergence of the gyroscopic pressure tensor and  $p_{\parallel,e}$  as well as  $p_{\perp,e}$  are the parallel and perpendicular electron pressure, respectively, given by moments of the gyro-center distribution function

$$p_{\parallel,sp} = \int d^3v m_{sp} v_{\parallel}^2 f_{sp}, \quad (16)$$

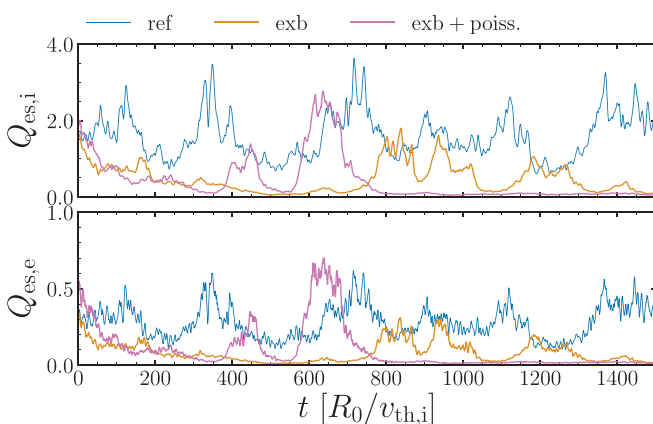


**FIG. 9.** Time traces of the ion- (top) and electron (bottom) electrostatic heat flux  $Q_{es,sp}$  (in units of  $\rho_*^2 n_0 T_0 v_{th,i}$ ) for the unmodified reference case (blue), a case without GA in the zonal  $E \times B$  nonlinearity (orange) and a case without GA both in the zonal  $E \times B$ -nonlinearity as well as the integral part of the Poisson equation (violet). All cases have  $R/L_T = 3.5$ .

$$p_{\perp,sp} = \int d^3v B \mu f_{sp}, \quad (17)$$

where  $\mu = m_{sp} v_{\perp}^2 / 2B$  is the magnetic moment. Equation (15) can be shown to apply well to the modified staircase states (see Fig. 14 in the Appendix). Given profiles of  $p_{\parallel,e}$  and  $p_{\perp,e}$  determine the parallel dependence of the electrostatic potential through Eq. (15). Curvature effects entering through  $\mathcal{K}_{\parallel}$  have similar magnitude compared to the parallel pressure and parallel electric field term (see Fig. 14) and, therefore, might introduce a variation of the electrostatic potential along  $s$ . The amplitude of the pressure and curvature terms, however, is small enough to introduce only a small relative variation of the electrostatic potential along  $s$  of

$$\Delta\phi = \frac{\max_s(\delta\phi) - \min_s(\delta\phi)}{\max_{\psi}(\langle\phi\rangle)} \sim 3\% - 4\% \quad (18)$$

in the case of a modified staircase, where  $\delta\phi = \phi - \langle\phi\rangle$  defines the  $s$ -varying part of  $\phi$  and  $\max_s/\min_s$  denotes maximum/minimum with respect to  $s$ . The electrostatic potential can, therefore, be considered constant on a flux surface in good approximation. And as a consequence, ZF structures deduced from the director field diagnostic at the LFS represent the zonal  $E \times B$ -flow on the whole flux surface. The solution of the parallel electron force balance  $\phi(\psi, s) = \delta\phi(\psi, s) + C$  determines the electrostatic potential up to a constant  $C$  with respect to  $s$  and, hence, leaves the zonal part of the electrostatic potential  $C = \langle\phi\rangle$  undetermined.

The zonal potential is related to plasma rotation and pressure through the radial ion force balance, which has found application in gyrokinetic studies.<sup>36,38,39</sup> In the local limit ( $\rho_* \rightarrow 0$ ) the flux surface averaged form can be written (see the Appendix)

$$0 = \nabla_{\psi} \langle\phi\rangle + [\nabla_{\psi} \langle p_{\perp,i} \rangle + \langle (\nabla \cdot \Pi_i)_{\psi} \rangle] - \langle (2\mathbf{u}_i \times \mathbf{B})_{\psi} \rangle, \quad (19)$$

where  $\nabla_{\psi} = \partial_{\psi}$  is the radial gradient,  $\mathbf{u}_i$  is the perturbed ion velocity and  $(\nabla \cdot \Pi_i)_{\psi}$  is the radial component of the divergence of the ion gyroviscous pressure tensor.

The radial gradient of the ion perpendicular pressure exhibits a distinct corrugated structure [see the exemplary cases with  $R/L_T = 3.75$  (left panels) and  $R/L_T = 6.9$  (right panels) in Fig. 10], with the radial location of the corrugations correlating with LORLs (vertical dotted lines) similar to Refs. 36 and 40. A variation along  $s$  is apparent, manifesting itself in positive radial corrugations at the LFS (orange dashed line in the mid panels) and negative mesoscale corrugations when averaging over the flux surface (blue solid line). This observation might relate to the perpendicular pressure component of Rosenbluth–Hinton residuals with reduced radial scale showing a similar poloidal variation,<sup>39</sup> or to the ballooning nature of the underlying ITG turbulence.<sup>33</sup> A further characteristic of the pressure corrugations is the radial asymmetry in the case of  $R/L_T = 3.75$  and the more symmetric appearance in the strong turbulent case with  $R/L_T = 6.9$  with respect LORLs.

Now, individual terms of the radial force balance [Eq. (19)] are evaluated for the cases depicted in Fig. 10. The  $\nabla_{\psi} \langle\phi\rangle$  term exhibits fine scale variations (violet dotted lines in the bottom panels of Fig. 10), in accordance with the spike features in  $\omega_{E \times B}$ , which cannot be balanced by the smoother pressure gradient profile (green solid). It is the gyroviscous pressure tensor that becomes relevant on scales comparable to the Larmor radius<sup>41</sup> and it will therefore be assumed

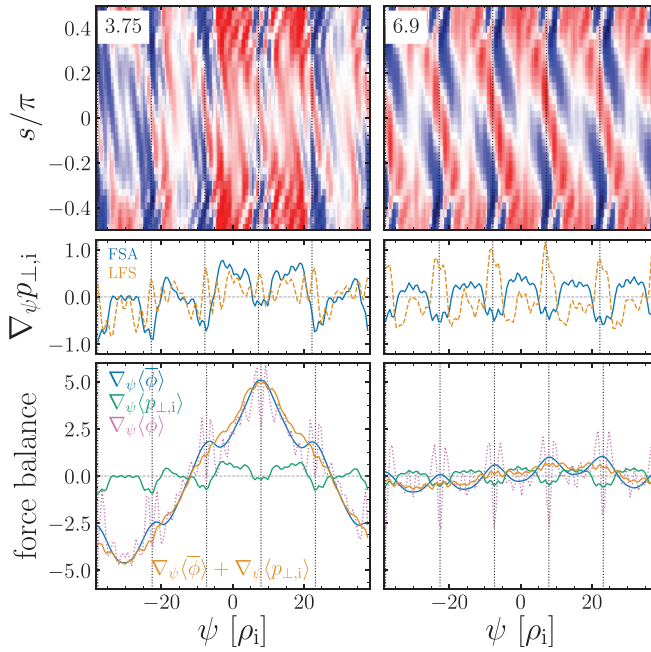


**FIG. 10.** Top panels: Radial gradient of the ion perpendicular pressure  $\nabla_\psi p_{\perp,i}$  ( $k_\zeta = 0$  component) in the  $\psi$ - $s$ -plane. The data are normalized to its maximum value and the color scale ranges linearly  $\in [-1.05, +1.05] \rightarrow [\text{blue, red}]$ . Mid panels: Radial profiles of the same quantity averaged over the flux surface (FSA) and at the low field side (LFS). Bottom panels: Flux-surface and time averaged radial profiles of  $\nabla_\psi\langle\bar{\phi}\rangle$  (blue),  $\nabla_\psi\langle p_{\perp,i}\rangle$  (green),  $\nabla_\psi\langle\phi\rangle$  (violet dotted) and  $\nabla_\psi\langle\bar{\phi}\rangle + \nabla_\psi\langle p_{\perp,i}\rangle$  (orange). The left panels represent a modified staircase state at  $R/L_T = 3.75$  and the right panels the strong turbulence reference case at  $R/L_T = 6.9$ .

that fine scale variations in the radial electric field term are compensated by the  $\langle(\nabla \cdot \Pi)_\psi\rangle$ -term. This assumption is supported by the observation that the gyroaverage mitigates the  $E \times B$ -flow connected to fine scale features (see Sec. III B 3) and motivates the formal introduction of a corrected electrostatic potential through

$$\nabla_\psi\langle\bar{\phi}\rangle \equiv \nabla_\psi\langle\phi\rangle + \langle(\nabla \cdot \Pi_i)\rangle_\psi. \quad (20)$$

The corrected zonal potential  $\langle\bar{\phi}\rangle$  is estimated using the director field under the following assumptions: (i) The director field is assumed to be proportional to the radial gradient of the advecting ZF velocity, i.e.,  $K_\phi - \langle K_\phi \rangle_\psi \propto \nabla_\psi v_{ZF}$ , which is justified by the director field calibration (Fig. 5). (ii) The spike features in the electrostatic potential do hardly contribute to the advection by the  $E \times B$ -drift and therefore the advecting ZF velocity is assumed to result from the corrected electrostatic potential  $v_{ZF} \propto \nabla_\psi\langle\bar{\phi}\rangle/2$ . Through radial integration of the director field one then obtains

$$\int K_\phi(\psi') - \langle K_\phi(\psi') \rangle_\psi d\psi' = \alpha_{\text{sim}} \nabla_\psi\langle\bar{\phi}\rangle(\psi)/2, \quad (21)$$

where  $\alpha_{\text{sim}}$  is a proportionality constant which is determined by fitting a linear function to Eq. (21) with the potential on the right hand side being replaced by the unmodified zonal electrostatic potential  $\langle\phi\rangle$ . Hence,  $\alpha_{\text{sim}}$  serves as a rescaling factor ensuring the corrected and

unmodified electrostatic potential being of the same order, i.e.,  $\langle\bar{\phi}\rangle \sim \langle\phi\rangle$  (compare blue solid and violet dotted line in the bottom left panel of Fig. 10). Comparison of the proportionality constants obtained in the director field calibration (Table II) and the here obtained  $\alpha_{\text{sim}} = 8.18 \text{ rad} \cdot R_0/v_{\text{th},i}$  demonstrates that  $\alpha_{\text{cal}} \approx \alpha_{\text{sim}}$  as expected.

When applying the above procedure a connection of the corrugations in  $K_\phi$  to “bump-dip”-like modulations of the estimated zonal flow velocity  $v_{ZF} \propto \nabla_\psi\langle\bar{\phi}\rangle/2$  (see blue line in Fig. 10) is identified. Summation of the estimated corrected electric field term and the ion pressure term of the radial force balance (orange solid line) eliminates these structures remarkably well, despite the crude approximations made above. This demonstrates that corrugations in  $K_\phi$  are related to flux surface averaged perpendicular pressure corrugations.

Some cautious words are in order regarding the evaluation of the pressure through the gyrocenter distribution function  $f$  [see Eqs. (16) and (17)] instead of the formally correct evaluation with the Vlasov particle distribution function  $F_V$  [see Eqs. (A6) and (A7)]. This approach requires the considered length scales to be significantly larger than the Larmor radius; which is also a requirement for validity of the here applied gyrotropic pressure tensor.<sup>41</sup> It is, therefore, justified in the description of the mesoscale corrugations with a spatial scale of  $\sim L_\psi/i_k \sim 10^1 \rho_i$ .

A similar overall conclusion can be drawn in the case of  $R/L_T = 6.9$  (right panels of Fig. 10). Since the random phase distribution of the mesoscale ZF component in this case (see Fig. 2) results in a strongly reduced amplitude of the  $n_{ZF} = 1$  component in  $\nabla_\psi\langle\phi\rangle$  when averaging over time, the fitting procedure introduced above is not applicable here. Instead, it is reasonable to set  $\alpha_{\text{sim}} = \alpha_{\text{cal}} = 4.8$  (compare Table II). This choice again successfully eliminates the corrugations in  $\nabla_\psi\langle\bar{\phi}\rangle$  (orange solid line).

Finally, it is noted that the quantitative agreement of the force balance under utilization of the reasonably rescaled director field and a physically meaningful moment of the distribution function can be considered a validation of the director field method applied to radially varying zonal  $E \times B$  flows.

## 5. Mesoscale pattern decomposition

Section II suggests that modified staircase structures can be understood as a superposition of a mesoscale  $n_{ZF} = 1$  component and pressure gradient related ZF corrugations. This section provides a decomposition of the modified staircase structure into the staircase (sc) and corrugation (corr.) component and aims to estimate the shear related to both components of the pattern.

The decomposition  $\langle\bar{\phi}\rangle = \langle\phi\rangle_{\text{sc}} + \langle\bar{\phi}\rangle_{\text{corr.}}$  is defined by

$$\nabla_\psi\langle\bar{\phi}\rangle_{\text{corr.}} = -\nabla_\psi\langle p_{i,\perp}\rangle \quad (22)$$

and the identification of  $\langle\bar{\phi}\rangle$  with the estimated corrected potential of Eq. (21). The shearing rate  $\bar{\omega}_{\text{ExB}}$  connected to the so obtained staircase and corrugation component is computed using Eq. (5) and is depicted by thin dashed lines in Fig. 11. Small scale variations in the pressure gradient (see mid and bottom panels of Fig. 10) result in spike structures in  $\bar{\omega}_{\text{ExB}}$  after radial derivation and a radial midpoint average is applied (solid lines) to allow for some degree of smoothing. The midpoint average of a quantity  $G$  is defined by

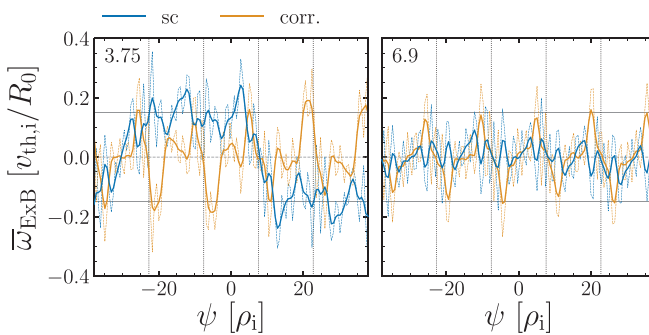


**FIG. 11.** Decomposition of the corrected shearing rate  $\bar{\omega}_{E\times B}$  into the staircase (blue dashed) and corrugation (orange dashed) part for  $R/L_T = 3.75$  (left) and  $R/L_T = 6.9$  (right). Solid lines depict the respective midpoint averaged profiles  $\langle \bar{\omega}_{E\times B} \rangle_W$ . The typical shearing rate of  $0.15 v_{th,i}/R_0$  is denoted by horizontal gray lines while vertical dotted lines depict LORLs.

$$\langle G \rangle_W(\psi_i) = \frac{1}{N} \sum_{j=-W}^W \mathcal{W}_j G(\psi_{i+j}) \quad (23)$$

with the normalization  $N = W + 1 + 2 \sum_{j=1}^W j$  and the weighting factor  $\mathcal{W}_j = W + 1 - |j|$ . Here,  $W = 2$  is chosen as a compromise between the smoothing of small scale variations, while retaining the corrugated structures.

The modified staircase state (left panel) is composed of a conventional staircase like structure (blue profile), i.e., a mesoscale structure in the shearing rate with extended radial intervals exhibiting a characteristic shearing rate and steep flanks at the zero crossings,<sup>19</sup> and corrugations in the shearing rate in the vicinity of LORLs (orange profile). Most notably, the characteristic mesoscale shear of  $\sim 0.15 v_{th,i}/R_0$  discussed in Sec. III A 3, here, agrees with the amplitude of both the staircase and the corrugated structures (horizontal gray line in Fig. 11). This structure composition and characteristic amplitude is observed over a wide range  $R/L_T \in [3.5, 3.75, 4.0, 4.5, 5.0]$ .

In the strong turbulence case (right panel) the staircase component is absent and the corrugations now appear as symmetric bipolar shear layers centered about LORLs. Hence, a qualitative change from asymmetric corrugations observed close to the threshold (left panel) to symmetric shear layers far away from the threshold (right panel) is found in agreement with the director field profiles shown in Fig. 6. This outcome highlights that the shear provided by corrugations and the underlying staircase structures is not merely additive. Rather, the shape of electrostatic potential around rational layers is changed in the presence of a staircase.

Finally, it is stressed that the shearing rate connected to the corrugations discussed here is directly related to a physically meaningful moment of the distribution function rather than to a quantity like the director field that requires a calibration.

### C. Interplay of modified staircase structures, $E \times B$ background shear flows and turbulent heat transport

Sections III A and III B demonstrate the emergence of mesoscale modified staircase structures whose interplay with a constant background  $E \times B$  shear is now investigated. Here, the background shear flow is intended to model sheared mean  $E \times B$  flows varying on the

radial scale of the machine size rather than that of the modified staircase structure. A sufficiently high time and radial resolution, required when applying a background shear,<sup>16</sup> has been ensured in a convergence study. Furthermore, the spatiotemporal organization of turbulent heat transport in the presence of sheared  $E \times B$  flows, i.e., both the modified staircase state and background shear, is discussed.

#### 1. Non-monotonic dependence of the turbulent heat transport on the background shear

Sheared background  $E \times B$  flows are considered to have a stabilizing effect on turbulence.<sup>6</sup> By contrast, here, an increase in the background shear  $\gamma_E$  does not necessarily reduce the transport level (see Fig. 12). Instead, two regimes with respect to  $\gamma_E$  can be identified:

- (I) In the limit of small background shear the dependence of the heat conductivity on the background shear is non-monotonic. After an initial increase with  $\gamma_E$  it eventually decreases and crosses the zero shear transport level (horizontal dotted lines). In this regime a sheared background flow does not cause stabilization with respect to the zero shear limit. Similar results have been obtained recently in a flux driven adiabatic model<sup>42</sup> and is interpreted as resulting from the interplay of staircase structures with a torque induced sheared rotation in the aforementioned reference. Indeed, some aspects of this effect might be present in recent studies in the ASDEX Upgrade experiment, reporting that an increase of the  $E \times B$  shear did not result in a confinement improvement.<sup>43</sup>
- (II) In a subsequent regime the heat conductivity decreases monotonically with  $\gamma_E$ . However, not all  $R/L_T$ -realization depicted in Fig. 12 exhibit this second regime. In the case of  $R/L_T = 4.0$  rather a sharp drop to zero transport level is found introducing a bivalent behavior of  $\chi_{es,i}(\gamma_E)$ . The transport level in the case of  $R/L_T = 3.5$  is too small to allow for a clear sharp drop.

The critical shearing rate  $\gamma_E^c \approx 0.1 - 0.15 v_{th,i}/R_0$  connected to both the transition from regime (I) to (II) as well as the drop in the transport level agrees well with typical shearing rates in the mesoscale

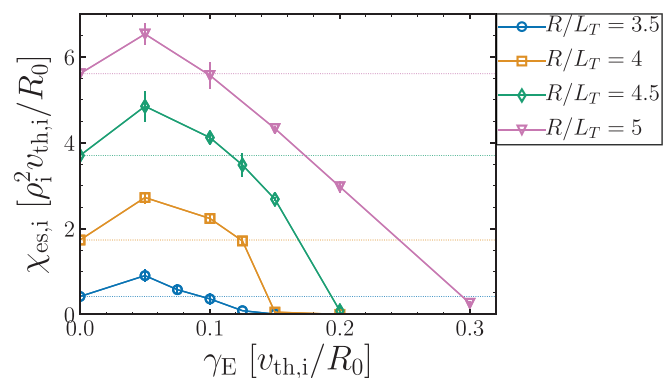


**FIG. 12.** Volume and time averaged electrostatic ion heat conductivity  $\chi_{es,i}$  against the background  $E \times B$  shearing rate  $\gamma_E$  for various values of  $R/L_T$ . Horizontal dotted lines depict the zero shear transport level.

( $n_{ZF} = 1$ ) ZF component (see Figs. 3 and 11) and the ZF corrugations (Fig. 11). In agreement with Ref. 42, the above observation is therefore interpreted as a manifestation of an interplay of modified staircase structures with the background shear flow.

This interpretation is supported by an investigation of zonal flow structures analyzed through the director field  $K_\phi$  (orange data in the right panels of Fig. 13). In regime (I) of  $R/L_T = 4.0$  a finite shear of  $\gamma_E = 0.1 v_{th,i}/R_0$  [panel (b)] results in regions with positive director field developing at the expense of negative plateaus of the modified staircase in the zero shear limit [panel (a)]. Similar to Ref. 42 the imposed background shear does not simply add to the shear connected to the modified staircase structures, i.e., the structure in the right panel of Fig. 6(b) does not result from a shift of the structure displayed in the right panel of (a) by a positive constant. Rather a transformation in the overall structure occurs with the maximum local value of the director field and, hence, the maximum shearing rate, being preserved. The most prominent observation is the occurrence of

mesoscale structures with zero crossings in the director field for the  $\gamma_E = 0.1 v_{th,i}/R_0$  case and their absence in the quenched state at  $\gamma_E = 0.2 v_{th,i}/R_0$  [panel (c)]. This observation suggests that the reduced shear at zero crossings of the director field allow for instabilities to grow locally<sup>34,44</sup> leading to the finite turbulent level. In the latter case the level of background shear exceeds typical shearing rates connected to modified staircase structures. As a result no zero crossnings in  $K_\phi$  are found and the radially finite positive shear is sufficient to suppress instabilities. Note that in this quenched case  $K_\phi$  does not exhibit ZF corrugations close to LORLs, showing that turbulence has to be active to sustain such structures.

At sufficiently large  $R/L_T$  zero crossings of the shearing rate are, however, not necessary for a finite turbulent level [see panel (d) in Fig. 13]. In the case of  $R/L_T = 5$  and  $\gamma_E = 0.2 v_{th,i}/R_0$  which is representative for regime (II) the director field is always larger than zero. Although signatures of ZF corrugations are visible, the shearing rate connected to those structures does not drop to zero.

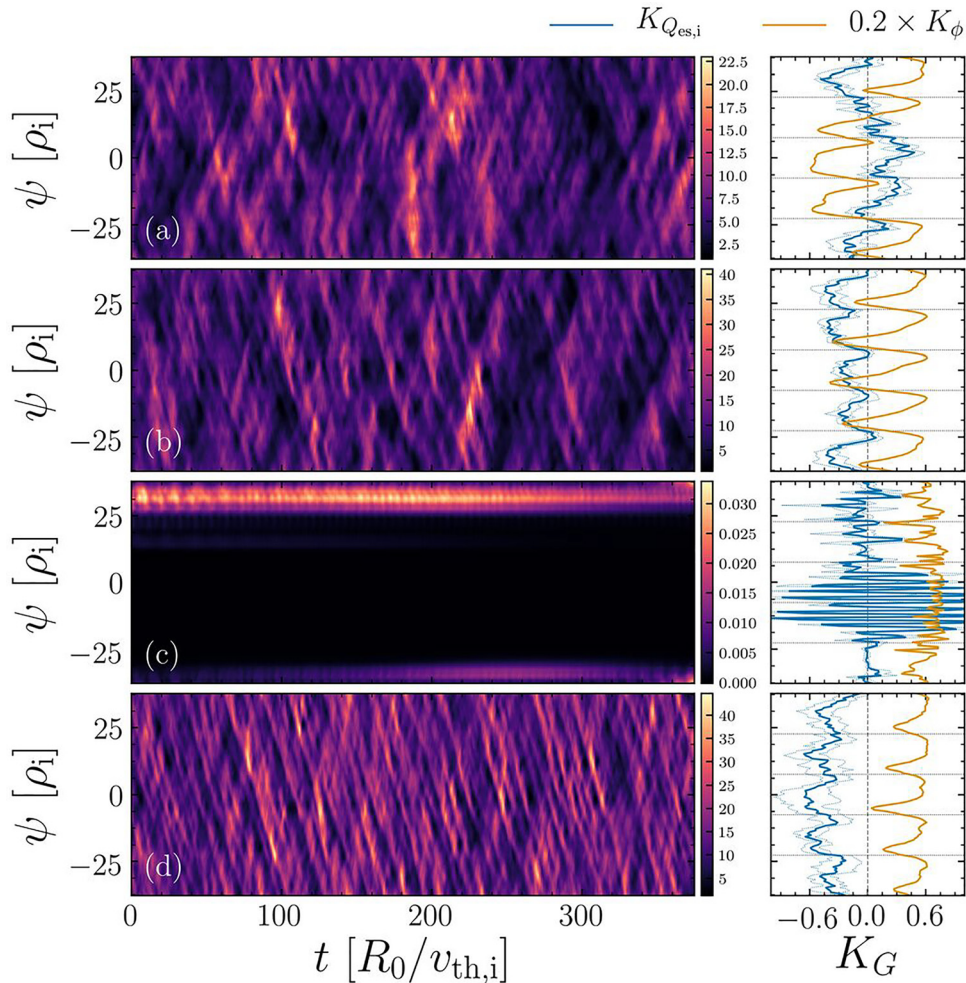


**FIG. 13.** Left: Flux-surface averaged electrostatic ion heat flux  $Q_{es,i}$  in the  $\psi$ - $t$ -plane for  $R/L_T = 4.0$  and  $\gamma_E = 0$  (a),  $\gamma_E = 0.1 v_{th,i}/R_0$  (b) and  $\gamma_E = 0.2 v_{th,i}/R_0$  (c) and for  $R/L_T = 5.0$  and  $\gamma_E = 0.2 v_{th,i}/R_0$  (d). Right: Corresponding temporally averaged radial profiles of the director fields  $K_{Q_{es,i}}$  (blue) and  $K_\phi$  (orange). Horizontal black dotted lines indicate LORLs.

## 2. Spatio-temporal organization of avalanche like transport events in the presence of modified staircase states and background shear flows

Turbulence close to marginal stability is often connected to avalanche like transport.<sup>45–47</sup> Avalanches are ballistically propagating transport events which organize spatially in the presence of an  $E \times B$ -staircase<sup>17,18</sup> as their propagating direction is anti-correlated with the sign of the local  $E \times B$  shearing rate.<sup>26,48,49</sup>

Due to their ballistic propagation, such transport events appear as inclined structures in the spatiotemporal representation ( $\psi$ - $t$ -plane) of turbulent fields. Treating avalanches as local pattern with the orientation representing the propagation direction and speed, allows for their detection through director field methods. Since heat avalanches are considered here the director field of the flux-surface averaged turbulent ion electrostatic heat flux  $K_{Q_{es,i}}$  is investigated (blue profiles in right panels of Fig. 13). Its definition follows Sec. II B with  $\zeta \rightarrow t$  as well as  $G = Q_{es,i}$  and positive (negative) values denote preferential outward (inward) propagation. An error is estimated by the standard deviation of  $K_{Q_{es,i}}$  calculated for six equally long temporal sub-intervals from the total time interval (thin blue dotted lines).

Although avalanche like transport events are visible in the spatiotemporal evolution of  $Q_{es,i}$  corresponding to a modified staircase state [panel (a) in Fig. 13], the spatial scale over which single events correlate appears significantly smaller than the  $n_{ZF} = 1$  mesoscale as usually observed in connection to staircases in local gradient-driven simulations with adiabatic electrons.<sup>19,21</sup> The propagation pattern especially lacks the clear radial location with respect to the  $n_{ZF} = 1$  mesoscale where avalanches are initiated. More in detail, Refs. 18, 19, and 21 find avalanches starting at the zero crossing of the  $n_{ZF} = 1$  structure where the shearing rate changes sign  $\omega_{E \times B} > 0 \rightarrow \omega_{E \times B} < 0$  with increasing radial coordinate and a subsequent inward (outward) propagation through regions with positive (negative)  $E \times B$  shear. The director field  $K_{Q_{es,i}}$ , however, demonstrates that there is an organization of the averaged avalanche propagation direction with respect to the  $n_{ZF} = 1$  mesoscale ZF [see right panel (a)]. The anti-correlation of  $K_{Q_{es,i}}$  and  $K_\phi$  is in agreement with literature and so is the preferential triggering of avalanches close to the zero crossing of the director field satisfying  $K_\phi > 0 \rightarrow K_\phi < 0$  with increasing radial coordinate (note that  $K_\phi$  is proportional to the local shearing rate). Therefore, both disparate mesoscales that are characteristic for the modified staircase state are manifest in the spatial organization of avalanches. This outcome confirms that avalanche like transport in connection with modified staircase states share similarities with their adiabatic counterpart.

The finite background shear cases [panel (b) and (d)] both exhibit preferentially inward propagating avalanches in agreement with the director field  $K_\phi$  being positive over almost the entire radial domain. The fact that  $K_{Q_{es,i}}$  approaches zero close to LORLs in the case of  $R/L_T = 4.0$  and  $\gamma_E = 0.1 v_{th,i}/R_0$  suggests that avalanche like transport dynamics is significantly organized with respect to the ZF corrugations. This claim is supported by the avalanche events visible in panel (b) of Fig. 13 being organized on a lengths scale of  $L_\psi/i_k$  with the triggering of individual events close to LORLs. In the case of  $R/L_T = 5.0$  and  $\gamma_E = 0.2 v_{th,i}/R_0$  [panel (d)], by contrast, the radial structuring of avalanches on corrugation scale is less obvious. Single avalanches rather travel (multiple times) over the entire radial domain, which manifests itself in a clear non-zero negative profile of  $K_{Q_{es,i}}$ .

Although, the triggering of individual avalanches close to LORLs cannot be identified, an interaction of avalanches with ZF corrugations in this case is nevertheless visible in form of an  $i_k$ -fold modulation in  $K_{Q_{es,i}}$ .

The above observations support the hypothesis that instabilities and the resulting turbulence is influenced by modified staircase in regime (I) but less in regime (II). In order to clarify the role of modified staircase for turbulence generating instabilities an stability analysis of modified staircase equilibria would be necessary, which is beyond the scope of this work.

## IV. CONCLUSION

Microturbulence close to marginality with inclusion of kinetic electrons<sup>24</sup> has been revisited. This work focused on the detection of mesoscale sheared zonal  $E \times B$  flow structures and on the comparison of such structures with fine scale features typically dominating the  $E \times B$  shearing rate when including electron dynamics.<sup>22,24</sup> The main results are summarized below.

Mesoscale modes in the zonal potential develop on considerable time scales of the order of  $\sim 10^2 - 10^3 v_{th,i}/R_0$ . An interplay of those mesoscale modes with lowest order rational layers is observed in the form of a radial lock-in behavior with  $i_k$ -fold symmetry. In contrast to fine scale features in the  $E \times B$  shearing rate whose amplitudes exceed typical growth rates by an order of magnitude, the  $E \times B$  shearing rate connected to the mesoscale modes follows the Waltz rule  $\omega_{ExB} \sim \gamma^{7,14}$  and is therefore physically meaningful.

In this paper the director field method<sup>25</sup> has been used to directly obtain a measure of the tilting of the eddy structures. It has been shown that the director field can be used to estimate the  $E \times B$  shearing rate provided the latter is connected to structures with a sufficient radial extent. The diagnostic shows that small scale  $E \times B$  shearing does not result in eddy tilting and, therefore, not in turbulence suppression. This observation is mainly attributed to finite Larmor radius effects that mitigate the ability of fine scale features to efficiently shear turbulent structures. The director field method reveals zonal flow mesoscale pattern formation on two distinct scales; namely, (i) mesoscale corrugations in the vicinity of lowest order rational layers and (ii) a mesoscale variation on the length scale of the radial boxsize. The lock-in of mesoscale zonal potential signatures is manifest in a distinct radial orientation of the latter structure. The amplitude of both structures can be related to typical shearing rates of a few  $\sim 10^{-1} v_{th,i}/R_0$ . Parallel and radial force balance relate the mesoscale corrugations occurring close to lowest order rational layers to perpendicular ion pressure corrugations. A structure decomposition based on the radial force balance demonstrates that the mesoscale pattern in the director field can be understood as being composed of a fully-developed type staircase<sup>19,21</sup> and pressure related zonal  $E \times B$  flow corrugations. The shape of the electrostatic potential around lowest order rational layers is influenced by the presence of a modified staircase, manifesting itself in a radial asymmetry of the zonal flow corrugations.

The combined effect of modified staircase structures and a background  $E \times B$  shear flow result in a non-monotonic dependence of the turbulent level on the background  $E \times B$  shearing rate. No shear stabilization is observed when the background shearing rate is smaller or comparable to the shearing rate connected to modified staircase structures. Similar observations in connection to the  $E \times B$ -staircase state have been made within a flux-driven model in Ref. 42. A director field

analysis of the turbulent heat flux demonstrates a spatiotemporal organization of heat avalanches with respect to the modified staircase structure. The averaged propagation direction of avalanches is anticorrelated with the local sign of the  $E \times B$  shearing rate<sup>26,48,49</sup> and the resulting averaged propagation pattern within the modified staircase is in agreement with heat avalanches in connection to the conventional  $E \times B$ -staircase state.<sup>17,18</sup>

The implications of this work are now briefly discussed. (i) The long-term dynamics introduced by slowly evolving mesoscale modified staircase state requires long time integration to accurately describe turbulent states close to the threshold. This requirement is computationally highly demanding when treating electrons as a kinetic species. The understanding of turbulence close to the threshold is, however, necessary since future reactors will operate close to marginal stability.<sup>50</sup> (ii) The  $E \times B$  shearing rate  $\omega_{E \times B}$ , i.e., the second radial derivative of the electrostatic potential, that is, often applied to characterize the shearing action of zonal flows, fails when structures on length scales of the Larmor radius dominate this observable. In this case director field methods provide a more accurate characterization of the shearing action of zonal  $E \times B$  flows since they are not biased by finite Larmor radius effects. (iii) Mesoscale  $E \times B$  staircase structures do develop in kinetic electron descriptions close to marginality even for CBC parameters. Hence fine scale features do not prevent staircases from developing. (iv) In contrast to the fully and partially developed variants of the  $E \times B$  staircase state observed in adiabatic electron models,<sup>19</sup> the modified form does not clearly exhibit a structure bifurcation. In particular, it does not allow for the transition of avalanche governed turbulent periods (partially developed staircase) to almost quenched periods (fully developed staircase) when CBC parameters are chosen. This type of turbulence dynamics, also observed in flux-driven near marginal turbulence with adiabatic electrons,<sup>18</sup> however, is recovered with the choice of a vanishing electron background temperature gradient. Inclusion of electron dynamics, therefore, bears additional physics that impacts near marginal turbulence and is therefore required to accurately describe such states.

## ACKNOWLEDGMENTS

Part of this work was performed using computational resources provided by the MARCONI-FUSION HPC.

## APPENDIX: PARALLEL AND RADIAL FORCE BALANCES IN THE PRESENCE OF A STRONG AND CURVED AMBIENT MAGNETIC FIELD

Here, parallel electron and radial ion force balance that are used in Sec. III B 4 are discussed. Starting point is the momentum density evolution equation following from taking moments of the Vlasov equation:<sup>41,51</sup>

$$\frac{\partial m_{sp} n_{sp} \mathbf{u}_{sp}}{\partial t} + \nabla \cdot (m_{sp} n_{sp} \mathbf{u}_{sp} \mathbf{u}_{sp}) + \nabla \cdot \mathbf{P}_{sp} - q_{sp} n_{sp} (\mathbf{E} + \mathbf{u}_{sp} \times \mathbf{B}) = 0, \quad (\text{A1})$$

where the index  $sp$  denotes the species. The stress tensor

$$\mathbf{P}_{sp} = m_{sp} \int (\mathbf{v} - \mathbf{u}_{sp})(\mathbf{v} - \mathbf{u}_{sp}) F_{V,sp} d^3 v, \quad (\text{A2})$$

the bulk velocity

$$\mathbf{u}_{sp} = \frac{1}{n_{sp}} \int \mathbf{v} F_{V,sp} d^3 v, \quad (\text{A3})$$

and the density

$$n_{sp} = \int F_{V,sp} d^3 v \quad (\text{A4})$$

enter Eq. (A1), where  $F_{V,sp}$  is the Vlasov particle distribution function,  $m_{sp}$  is the species mass and  $\mathbf{v}$  is the velocity space coordinate. In a strong ambient magnetic field the pressure tensor can be written as<sup>41,52</sup>

$$\mathbf{P}_{sp} = p_{\perp,sp} \mathbb{1} + (p_{\parallel,sp} - p_{\perp,sp}) \mathbf{b} \mathbf{b} + \boldsymbol{\Pi} \quad (\text{A5})$$

with the first two terms on the right hand side constitute the gyro-tropic pressure tensor  $\mathbf{P}_{sp}^g$ , and the last term, the gyroviscous stress tensor  $\boldsymbol{\Pi}$ , including finite Larmor radius effects.

The parallel and perpendicular pressure can be obtained from the pressure tensor by double contraction and read<sup>41</sup>

$$p_{\parallel,sp} = m_{sp} \int (v_{\parallel} - u_{\parallel})^2 F_{V,sp} d^3 v, \quad (\text{A6})$$

$$p_{\perp,sp} = \frac{m_{sp}}{2} \int |\mathbf{v}_{\perp} - \mathbf{u}_{\perp}|^2 F_{V,sp} d^3 v \quad (\text{A7})$$

with  $v_{\parallel}$  and  $\mathbf{v}_{\perp}$  being the velocity coordinates parallel and perpendicular to the magnetic field and  $u_{\parallel}$  and  $\mathbf{u}_{\perp}$  the respective bulk velocity components. It is the divergence of the pressure tensor

$$\nabla \cdot \mathbf{P}_{sp} = \nabla p_{\perp} + (p_{\parallel} - p_{\perp}) [\mathbf{b}(\nabla \cdot \mathbf{b}) + (\mathbf{b} \cdot \nabla) \mathbf{b}] \quad (\text{A8})$$

$$+ \mathbf{b}(\mathbf{b} \cdot \nabla)(p_{\parallel} - p_{\perp}) + \nabla \cdot \boldsymbol{\Pi} \quad (\text{A9})$$

that enters the momentum equation. The terms within the squared brackets describe magnetic curvature effects.

The  $\delta f$ -approximation applied in this work splits the distribution function into a background Maxwellian and a perturbed distribution  $F = F_M + f$  with  $F_M \sim \mathcal{O}(1)$  and  $f \sim \mathcal{O}(\rho_*)$ . Only the perturbed distribution  $f$  is evolved in the  $\delta f$ -approximation and the pressure entering the force balance equations below is formulated in terms of this latter distribution. The usual ordering  $\mathbf{u}_{sp}, \phi, n_{sp} \sim \mathcal{O}(\rho_*)$  and  $n_{0,sp}, \mathbf{B} \sim \mathcal{O}(1)$  is adopted, where  $n_{0,sp}$  is the species background density, i.e., the zeroth order moment over  $F_M$ . The equations below will be formulated in first order of  $\rho_*$  and therefore the second term of Eq. (A1) as well as the bulk velocity  $\mathbf{u}_{sp}$  contributions in Eq. (A2) are neglected.

The parallel electron force balance is obtained by the inner product of Eq. (A1) with the unit vector tangential to the ambient magnetic field  $\mathbf{b}$  together with  $q_e = -e$ . Its dimensionless and first order in  $\rho_*$  form reads

$$0 = \nabla_{\parallel} \phi - [\mathcal{K}_{\parallel}(p_{\parallel,e}, p_{\perp,e}) + \nabla_{\parallel} p_{\parallel,e}] \quad (\text{A10})$$

with normalization in units of  $\rho_i n_0 T_0 / R_0^2$ . The divergence of the gyroviscous pressure tensor has been neglected due to the small electron Larmor radius. Furthermore, the parallel gradient is

$$\nabla_{\parallel} = \mathbf{b} \cdot \nabla = \frac{\mathbf{B} \cdot \nabla s}{B} \frac{\partial}{\partial s} \quad (\text{A11})$$

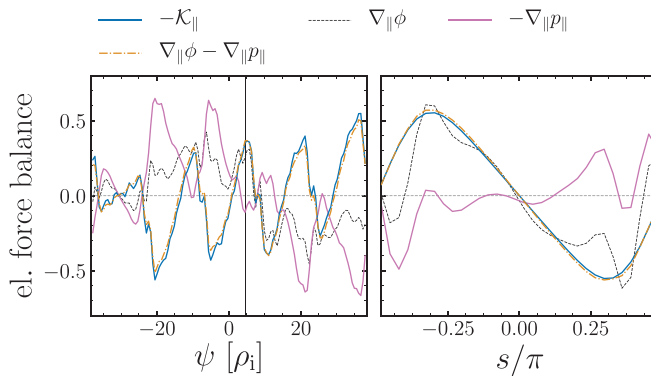


**FIG. 14.** Temporally averaged terms of the parallel electron force balance for a modified staircase state with  $R/L_T = 3.75$ . Shown are radial profiles averaged over a poloidal half turn  $s \in [-0.5, 0]$  (left) and  $s$ -profiles (right) for the radial location indicated by the vertical line in the left panel.

as well as

$$\mathcal{K}_{\parallel}(p_{\parallel,e}, p_{\perp,e}) = (p_{\parallel,e} - p_{\perp,e})(\nabla \cdot \mathbf{b}) \quad (\text{A12})$$

$$= -(p_{\parallel,e} - p_{\perp,e}) \frac{\mathbf{B} \cdot \nabla B}{B^2}, \quad (\text{A13})$$

which defines the curvature term. Curvature effects enter the lowest order electron parallel force balance since the scales connected to both the ambient magnetic field and the variation of perturbed quantities parallel to the magnetic field are of the machine size  $\sim R_0$ . The parallel force balance is well satisfied for the modified staircase state (Fig. 14). Note that parallel and perpendicular electron pressure are evaluated through the gyro-center distribution function  $f_{sp}$  according to Eq. (16).

The radial ion force balance is obtained by the inner product of the momentum equation [Eq. (A1)] with the radial unit vector  $\hat{\mathbf{e}}_r$  as well as  $q_i = +e$ . Its dimensionless and first order in  $\rho_*$  form reads

$$0 = \nabla_{\psi}\phi + [\nabla_{\psi}p_{\perp,i} + (\nabla \cdot \Pi_i)\psi] - 2(\mathbf{u}_i \times \mathbf{B})_{\psi} \quad (\text{A14})$$

with normalizations in units of  $n_0 T_0 / R_0$ . The normalized radial coordinate  $\psi = r/\rho_i$  and the notation  $\nabla_{\psi} = \partial_{\psi}$  have been introduced. The radial curvature term  $\rho_* \mathcal{K}_r(p_{\parallel,i}, p_{\perp,i}) = \rho_*(p_{\parallel,i} - p_{\perp,i}) \hat{\mathbf{e}}_r (\mathbf{b} \cdot \nabla) \mathbf{b}$  is of higher order in  $\rho_*$ . The factor  $\rho_*$  results from the ambient magnetic field varying on the machine size  $\sim R_0$ , while the radial variation of the perturbed quantities is of the size of the Larmor radius  $\sim \rho_i$ . In the local limit  $\rho_* \rightarrow 0$  the curvature term is negligible.

## DATA AVAILABILITY

The data that support the findings of this study are available from the corresponding author upon reasonable request.

## REFERENCES

- <sup>1</sup>Z. Lin, T. S. Hahm, W. W. Lee, W. M. Tang, and R. B. White, *Science* **281**, 1835 (1998).
- <sup>2</sup>R. E. Waltz and C. Holland, *Phys. Plasmas* **15**, 122503 (2008).
- <sup>3</sup>M. Nakata, T.-H. Watanabe, and H. Sugama, *Phys. Plasmas* **19**, 022303 (2012).
- <sup>4</sup>G. G. Whelan, M. J. Pueschel, and P. W. Terry, *Phys. Rev. Lett.* **120**, 175002 (2018).
- <sup>5</sup>W. A. Cooper, *Plasma Phys. Controlled Fusion* **30**, 1805 (1988).
- <sup>6</sup>H. Biglari, P. H. Diamond, and P. W. Terry, *Phys. Fluids B* **2**, 1 (1990).
- <sup>7</sup>R. E. Waltz, G. D. Kerbel, and J. Milovich, *Phys. Plasmas* **1**, 2229 (1994).
- <sup>8</sup>A. M. Dimits, G. Bateman, M. A. Beer, B. I. Cohen, W. Dorland, G. W. Hammett, C. Kim, J. E. Kinsey, M. Kotschenreuther, A. H. Kritz, L. L. Lao, J. Mandrekas, W. M. Nevins, S. E. Parker, A. J. Redd, D. E. Shumaker, R. Sydora, and J. Weiland, *Phys. Plasmas* **7**, 969 (2000).
- <sup>9</sup>T. S. Hahm and K. H. Burrell, *Phys. Plasmas* **2**, 1648 (1995).
- <sup>10</sup>K. H. Burrell, *Phys. Plasmas* **4**, 1499 (1997).
- <sup>11</sup>M. W. Shafer, R. J. Fonck, G. R. McKee, C. Holland, A. E. White, and D. J. Schlossberg, *Phys. Plasmas* **19**, 032504 (2012).
- <sup>12</sup>M. F. J. Fox, F. van Wyk, A. R. Field, Y.-C. Ghim, F. I. Parra, A. A. Schekochihin, and MAST Team, *Plasma Phys. Controlled Fusion* **59**, 034002 (2017).
- <sup>13</sup>J. R. Pinzón, T. Happel, P. Hennequin, C. Angioni, T. Estrada, A. Lebschy, U. Stroth, and ASDEX Upgrade Team, *Nucl. Fusion* **59**, 074002 (2019).
- <sup>14</sup>R. Waltz, R. Dewar, and X. Garbet, *Phys. Plasmas* **5**, 1784 (1998).
- <sup>15</sup>J. E. Kinsey, R. E. Waltz, and J. Candy, *Phys. Plasmas* **12**, 062302 (2005).
- <sup>16</sup>F. J. Casson, A. G. Peeters, Y. Camenen, W. A. Hornsby, A. P. Snodin, D. Strintzi, and G. Szepesi, *Phys. Plasmas* **16**, 092303 (2009).
- <sup>17</sup>G. Dif-Pradalier, P. H. Diamond, V. Grandgirard, Y. Sarazin, J. Abiteboul, X. Garbet, Ph. Ghendrih, A. Strugarek, S. Ku, and C. S. Chang, *Phys. Rev. E* **82**, 025401(R) (2010).
- <sup>18</sup>F. Rath, A. G. Peeters, R. Buchholz, S. R. Grosshauser, P. Migliano, A. Weikl, and D. Strintzi, *Phys. Plasmas* **23**, 052309 (2016).
- <sup>19</sup>A. G. Peeters, F. Rath, R. Buchholz, Y. Camenen, J. Candy, F. J. Casson, S. R. Grosshauser, W. A. Hornsby, D. Strintzi, and A. Weikl, *Phys. Plasmas* **23**, 082517 (2016).
- <sup>20</sup>G. Dif-Pradalier, G. Hornung, X. Garbet, Ph. Ghendrih, V. Grandgirard, G. Latu, and Y. Sarazin, *Nucl. Fusion* **57**, 066026 (2017).
- <sup>21</sup>A. Weikl, A. G. Peeters, F. Rath, S. R. Grosshauser, R. Buchholz, W. A. Hornsby, F. Seiferling, and D. Strintzi, *Phys. Plasmas* **24**, 102317 (2017).
- <sup>22</sup>J. Dominski, S. Brunner, T. Görler, F. Jenko, D. Told, and L. Villard, *Phys. Plasmas* **22**, 062303 (2015).
- <sup>23</sup>Y. Idomura, *Plasma Fusion Res.* **11**, 2403006 (2016).
- <sup>24</sup>A. Weikl, A. G. Peeters, F. Rath, F. Seiferling, R. Buchholz, S. R. Grosshauser, and D. Strintzi, *Phys. Plasmas* **25**, 072305 (2018).
- <sup>25</sup>D. A. Egolf, I. V. Melnikov, and E. Bodenschatz, *Phys. Rev. Lett.* **80**, 3228 (1997).
- <sup>26</sup>B. F. McMillan, S. Jolliet, T. M. Tran, L. Villard, A. Bottino, and P. Angelino, *Phys. Plasmas* **16**, 022310 (2009).
- <sup>27</sup>A. G. Peeters, Y. Camenen, F. J. Casson, W. A. Hornsby, A. P. Snodin, D. Strintzi, and G. Szepesi, *Comput. Phys. Commun.* **180**, 2650–2672 (2009).
- <sup>28</sup>S. Hamada, Kakuyugo Kenkyu **1**, 542 (1958).
- <sup>29</sup>G. Hornung, G. Dif-Pradalier, F. Clairet, Y. Sarazin, R. Sabot, P. Hennequin, and G. Verdoollaeghe, *Nucl. Fusion* **57**, 014006 (2017).
- <sup>30</sup>B. D. Scott, *New J. Phys.* **7**, 92 (2005).
- <sup>31</sup>M. J. Pueschel, M. Kammerer, and F. Jenko, *Phys. Plasmas* **15**, 102310 (2008).
- <sup>32</sup>J. W. Connor, R. J. Hastie, and J. B. Taylor, *Phys. Rev. Lett.* **40**, 396 (1978).
- <sup>33</sup>S. C. Cowley, R. M. Kulsrud, and R. Sudan, *Phys. Fluids B* **3**, 2767 (1991).
- <sup>34</sup>B. F. McMillan, P. Hill, A. Bottino, S. Jolliet, T. Vernay, and L. Villard, *Phys. Plasmas* **18**, 112503 (2011).
- <sup>35</sup>P. Migliano, R. Buchholz, S. R. Grosshauser, W. A. Hornsby, A. G. Peeters, and O. Stauffert, *Nucl. Fusion* **56**, 014002 (2016).
- <sup>36</sup>R. E. Waltz, M. E. Austin, K. H. Burrell, and J. Candy, *Phys. Plasmas* **13**, 052301 (2006).
- <sup>37</sup>X. Garbet, Y. Idomura, L. Villard, and T. H. Watanabe, *Nucl. Fusion* **50**, 043002 (2010).
- <sup>38</sup>A. M. Dimits, B. I. Cohen, W. M. Nevins, and D. E. Shumaker, *Nucl. Fusion* **40**, 1725 (2001).
- <sup>39</sup>O. Yamagashi, *Plasma Phys. Controlled Fusion* **60**, 045009 (2018).
- <sup>40</sup>J. Candy, *Phys. Plasmas* **12**, 072307 (2005).
- <sup>41</sup>P. Hunana *et al.*, *arXiv:1901.09354v2* (2019).
- <sup>42</sup>F. Seiferling, A. G. Peeters, S. R. Grosshauser, F. Rath, and A. Weikl, *Phys. Plasmas* **26**, 102306 (2019).
- <sup>43</sup>M. Reisner, E. Fable, J. Stober, A. Bock, A. Bañon Navarro, A. Di Siena, R. Fischer, V. Bobkov, R. McDermott, and ASDEX Upgrade Team, *Nucl. Fusion* **60**, 082005 (2020).

- <sup>44</sup>B. N. Rogers, W. Dorland, and M. Kotschenreuther, *Phys. Rev. Lett.* **85**, 5336 (2000).
- <sup>45</sup>P. H. Diamond and T. S. Hahm, *Phys. Plasmas* **2**, 3640 (1995).
- <sup>46</sup>X. Garbet and R. E. Waltz, *Phys. Plasmas* **5**, 2836 (1998).
- <sup>47</sup>P. A. Politzer, *Phys. Rev. Lett.* **84**, 1192 (2000).
- <sup>48</sup>Y. Idomura, H. Urano, N. Aiba, and S. Tokuda, *Nucl. Fusion* **49**, 065029 (2009).
- <sup>49</sup>M. J. Choi, H. Jhang, J.-M. Kwon, J. Chung, M. Woo, L. Qi, S. Ko, T.-S. Hahm, H. K. Park, and H.-S. Kim, *Nucl. Fusion* **59**, 086027 (2019).
- <sup>50</sup>J. Candy, “TGLF recalibration for ITER standard case parameters FY2015: Theory and simulation performance target final report,” Report No. GA-A-28239 (General Atomics, USA, 2015).
- <sup>51</sup>F. L. Hinton and R. D. Hazeltine, *Rev. Mod. Phys.* **48**, 239 (1976).
- <sup>52</sup>F. G. Chew, M. L. Goldberger, and F. E. Low, *Proc. R. Soc. A* **236**, 112 (1956).